1 **Title:** Cadherins regulate nuclear topography and function of developing ocular

2 motor circuitry

3

4 **Authors:** Athene Knüfer[1], Giovanni Diana[1], Gregory S. Walsh[2], Jonathan Clarke[1] and

5 Sarah Guthrie[3,*]

6

7 **Affiliations:** 1. Centre for Developmental Neurobiology, King's College London,

8 New Hunt's House, Guy's Campus, London SE1 1UL, United Kingdom

9 2. Department of Biology, Virginia Commonwealth University, 1000 West Cary

10 Street Suite 126, Richmond, VA 23284-2012, United States of America

11 3. School of Life Sciences, University of Sussex, JMS Building, Brighton BN7 9QG,

12 United Kingdom

13 *Correspondence: s.guthrie@sussex.ac.uk

14

15 **Abstract**

16 In the vertebrate central nervous system, groups of functionally-related neurons, including

17 cranial motor neurons of the brainstem, are frequently organised as nuclei. The molecular

18 mechanisms governing the emergence of nuclear topography and circuit function are poorly

19 understood. Here we investigate the role of cadherin-mediated adhesion in the development

20 of zebrafish ocular motor (sub)nuclei. We find that developing ocular motor (sub)nuclei

21 differentially express classical cadherins. Perturbing cadherin function in these neurons

22 results in distinct defects in neuronal positioning, including scattering of dorsal cells and

23 defective contralateral migration of ventral subnuclei. In addition, we show that cadherin-

24 mediated interactions between adjacent subnuclei are critical for subnucleus position. We

25 also find that disrupting cadherin adhesivity in dorsal oculomotor neurons impairs the larval

26 optokinetic reflex, suggesting that neuronal clustering is important for co-ordinating circuit

27 function. Our findings reveal that cadherins regulate distinct aspects of cranial motor neuron

28 positioning and establish subnuclear topography and motor function.

29
30
31
32
33
34
35
36

Introduction

During vertebrate embryonic development, neurons within the central nervous system (CNS) assemble into stereotyped anatomical structures, such as clusters or layers (laminae). Neurons which share common inputs and axonal outputs, including motor neurons of the brainstem and spinal cord, are often organised as coherent clusters of cells, termed nuclei. Despite their prevalence, little is known about the mechanisms regulating their development (nucleogenesis). The correct arrangement of motor neurons within nuclei is thought to be critical for multiple aspects of circuit formation, including muscle target innervation and acquisition of sensory inputs (Landmesser et al., 1978; Sürmeli et al., 2011). Consequently, understanding the molecular programmes that direct motor neuron positioning and assembly of functional neuromuscular circuits represents an important challenge.

In the brainstem, some cranial motor nuclei, such as the oculomotor nucleus and facial motor nucleus, can be further divided into subnuclei according to their efferent projections. Neurons that contribute axons to the same cranial nerve yet innervate different muscle targets exhibit stereotyped topography within the larger nucleus (Greaney et al., 2017; McArthur & Fetcho, 2017). To date, the molecular and cellular processes which give rise to subnuclear topography remain unknown. The positioning of some groups of motor neurons has been shown to be regulated by members of the classical cadherin superfamily of cell adhesion molecules, which include type I and type II cadherins (Price et al., 2002; Demireva et al., 2011; Astick et al., 2014; Dewitz et al., 2018; Dewitz et al., 2019). Differential expression of type II cadherins, which participate in homophilic as well as heterophilic interactions (Patel et al., 2006), drives the segregation and coalescence of somatomotor and branchiomotor neurons into discrete cranial motor nuclei (Astick et al., 2014). Furthermore, cadherins participate in an intricate network of interactions with gap junctions and spontaneous activity, which regulates the emergence of mature topography in brainstem motor nuclei (Montague et al., 2017). Whereas the role of cadherins in the segregation of different motor neuron subtypes has been investigated, their requirement for the development of subnuclear architecture or motor function is unclear.

The zebrafish ocular motor system, which comprises the oculomotor nucleus (nIII) of the midbrain, as well as the trochlear (nIV) and abducens nuclei (nVI) of the hindbrain, provides an unparalleled opportunity to address these questions. The anatomical layout of the system is well-conserved among vertebrates; together the three nuclei innervate six extraocular muscles responsible for coordinating important eye movements (Graf & McGurk, 1985; Evinger et al., 1988; Gilland and Baker, 2005). Four of these muscles are innervated by the four constituent subnuclei of nIII, whereas nIV and nVI each target a single muscle.

72   Oculomotor subnuclei are known to exhibit spatial topography with respect to muscle target,

73   segregated along the dorsoventral axis (Greaney et al., 2017); in higher vertebrates this

74   organisation also extends to the visceral motor neurons of the Edinger-Westphal nucleus

75   found dorsal of nIII (Hasan et al., 2010). Curiously, neurons belonging to the superior rectus

76   (SR) subnucleus are known to translocate their soma across the midline in an unusual

77   migration to the contralateral side (Puelles-Lopez et al., 1975; Naujoks-Manteuffel, 1991),

78   giving rise to contralateral connectivity.

79   In this study, we utilise the fine-grained anatomy and precise motor control of the zebrafish

80   ocular motor system to identify the contribution of cadherin-mediated adhesion to the

81   emergence of subnuclear topography and circuit function *in vivo*. We find that nIII subnuclei

82   differentially express repertoires of type I and type II cadherins. Cranial motor neuron-specific

83   perturbation of cadherin function interferes with normal programmes of neuronal positioning

84   specific to each subnucleus, such as the clustering of dorsal oculomotor neurons and

85   contralateral migration of ventral SR neurons. We also find that neurons belonging to the

86   adjacent IO subnucleus, in which cadherin function is unperturbed, are mispositioned,

87   suggesting that cadherin-mediated interactions between subnuclei contribute to their normal

88   positioning. Finally, we find that cadherin function in dorsal oculomotor neurons is required

89   for the development of efficient eye movements, as perturbing cadherin adhesivity impairs

90   the nasal eye movements of the oculomotor-driven optokinetic reflex (OKR) predictably. Our

91   findings show that cadherins play a fundamental role in the assembly of cranial motor

92   subnuclei and circuitry, and may facilitate the integration of motor neurons into functional

93   circuits by controlling their stereotyped positioning.

94

95

96

97

98

99

100

101

102

103

104

105

Results

Developing ocular motor neurons differentially express cadherin combinations

In addition to their established roles in controlling motor neuron topography (Price et al., 2002; Astick et al., 2014), recent work indicates that type II cadherins act synergistically with the type I cadherin cdh2 (N-Cadherin) to control their precise positioning, although the exact mechanism remains unclear (Dewitz et al., 2019). In order to determine whether type I and type II cadherins are plausible candidates to play a role in ocular motor neuron development, we assayed the expression of several cadherins in developing ocular motor neurons using RNAscope fluorescent in situ hybridisation. Cadherin transcript detection was performed in transgenic *Isl1:GFP* zebrafish embryos, in which the majority of ocular motor neurons, including trochlear (nIV) and most oculomotor (nIII) neurons are known to express GFP (Higashijima et al., 2000). nIII neurons innervating the inferior oblique (IO) muscle, as well as abducens (nVI) motor neurons, lack GFP expression; we therefore focussed our analyses on nIII and nIV neurons which are GFP-positive.

Isl1:GFP fluorescence was preserved following RNAscope processing, allowing expression of individual mRNAs to be examined in ocular motor neurons, which display a fanned arrangement during development, within the intact brain (Figure 1A). Due to the lack of subpopulation-specific markers, expression in nIII subnuclei was assayed based on their anatomical location, as neurons are generated and distributed along the dorsoventral (DV) axis stereotypically (Greaney et al., 2017; Figure 1B-C). Whereas the dorsal (and lateral) proportion of nIII contains motor neuron groups innervating inferior rectus (IR) and medial rectus (MR) muscles, ventral (and medial) nIII predominantly contains superior rectus (SR)-innervating neurons, as well as inferior oblique (IO) neurons just lateral of these (Greaney et al., 2017). Our data indicate that IO neurons are also found further dorsal, consistent with reports in other teleost species (Graf & McGurk, 1985; Luiten & Dijkstra-de Vlieger, 1978). Superior oblique (SO)-innervating neurons belonging to nIV are located proximal to and just rostral of nIII in rhombomere 1 (r1) of the hindbrain.

Expression of mRNAs was surveyed at 48 hpf, ~2hrs before neurogenesis is complete in both nuclei (Greaney et al., 2017), and 72 hpf, when all extraocular motor neuron branches have innervated their respective muscle targets (Clark et al., 2013). At 48 hpf, ocular motor neurons expressed combinations of cadherins (Figures 1B-C and Figure 1-figure supplement 1C-E), and differential expression was observed between dorsal and ventral nIII subnuclei, as well as between nIII and nIV. Detection was highly specific, as in situ hybridisation with a negative control probe against the bacterial mRNA *dapB* revealed almost no signal (Figure

4

141   Figure 1-figure supplement 1A), whereas expression of the transcription factor *foxg1a* within

142   the CNS was restricted to telencephalic regions consistent with its known expression pattern

143   (Figure 1–figure supplement 1B; Danesin et al., 2009). Previous work has shown that

144   selectivity of adhesion between cell types can be achieved by discrete profiles of cadherin

145   expression, as well as by varying levels of the same cadherin (Price et al., 2002; Steinberg &

146   Takeichi, 1994). We find that cadherin expression within ocular motor subnuclei and

147   surrounding non-motor neuron cell types varies both in intensity and spatial distribution. For

148   example, expression of the type I cadherin *cdh2* (N-Cadherin) and type II cadherin *cdh11*

149   was detected in all ocular motor neurons, displaying a broad and relatively uniform

150   distribution across subnuclei, as well as cells immediately surrounding them (Figure 1D and

151   1H; Figure 1-figure supplement 1D). Based on anatomical location, GFP-negative IO neurons

152   therefore likely also express *cdh2* and *cdh11*, in addition to GFP-expressing ocular motor
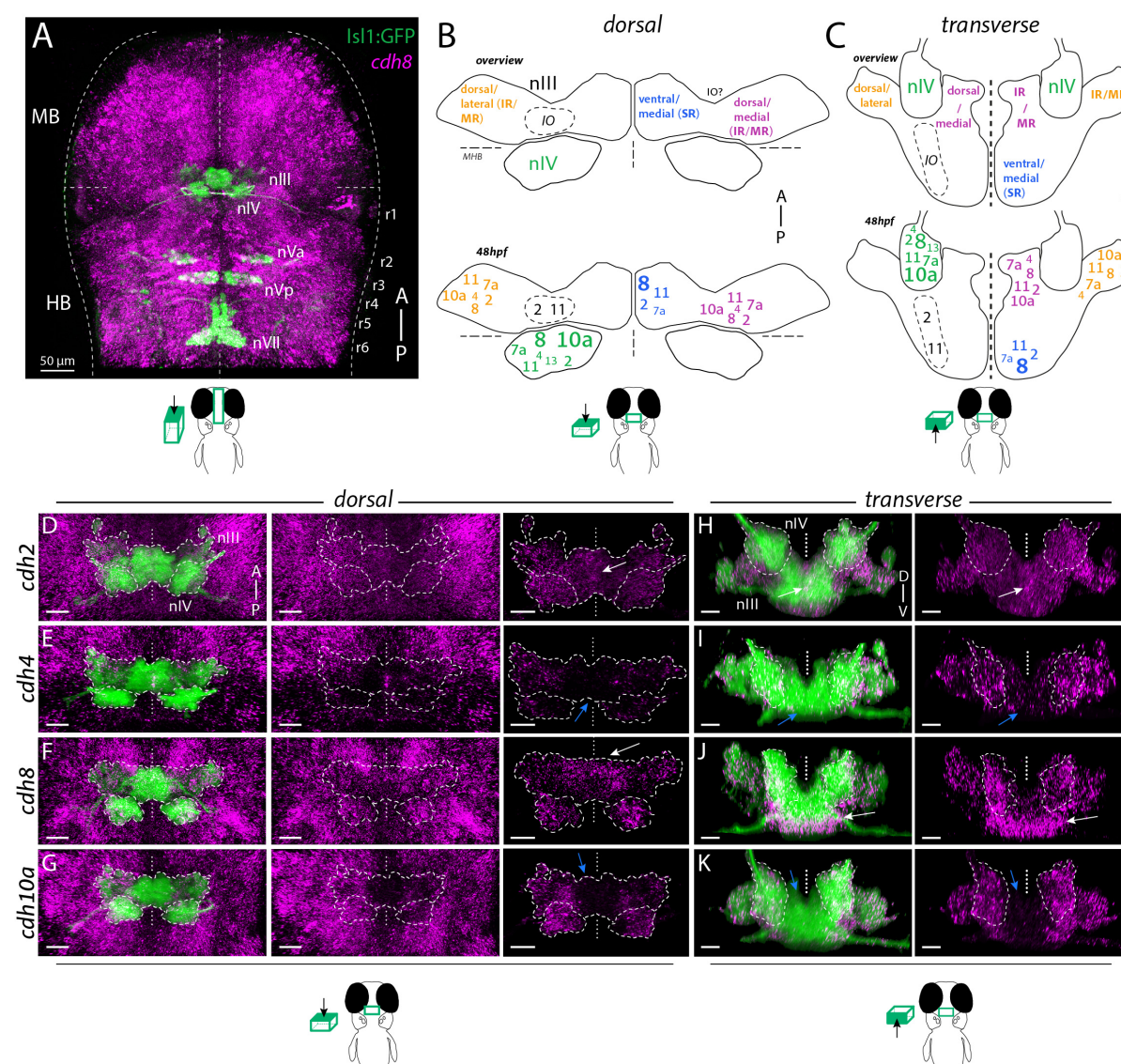
153   neurons.

154

155   Figure 1.

156   Other cadherins exhibited more restricted expression patterns, with marked differences
157   observed between dorsal and ventral nIII. Dorsal subnuclei expressed several cadherins,
158   including *cdh4* (type I; Figures 1E and 1I) and *cdh10a* (type II; Figures 1G and K), which
159   exhibited no or negligible expression in ventromedial nIII. In contrast, other cadherins were
160   expressed by all nIII neurons but to varying degrees: expression of *cdh8* (type II; Figures 1F
161   and 1J; Movie 1) was far higher in ventral than in dorsal nIII, whereas *cdh7a* expression (type
162   II; Figure 1-figure supplement 1C; Movie 2) was lower in ventral neurons compared to dorsal
163   nIII neurons. At 72 hpf, ocular motor neurons continued to express cadherin combinations
164   (Figures 1-figure supplement 2A-I), with continued broad expression of *cdh2* and *cdh11*,
165   however several cadherins showed higher expression in nIII, most notably *cdh4* (Figure 1-
166   figure supplement 2D) and *cdh13* (Figure 1-figure supplement 2I). Despite this, differential
167   expression between dorsal and ventral nIII was maintained: expression of *cdh10a* remained
168   absent from the most medial part of ventral nIII (Figure 1-figure supplement 2G), whereas
169   expression of *cdh8* was higher compared to dorsal nIII (Figure 1-figure supplement 2F). IO
170   neurons may also differentially express additional type II cadherins which display less uniform
171   expression, although their lack of *Isl1:GFP* expression prevents us from evaluating this
172   definitively. In sum, 2/7 cadherins surveyed showed general expression within ocular motor
173   nuclei at both developmental stages, whereas the remaining cadherins displayed differential
174   and dynamic expression across (sub)nuclei. These results reveal a complex organisation of
175   cadherin expression in developing ocular motor neurons, whereby dorsal and ventral ocular
176   motor subnuclei are defined by unique combinations of cadherin expression during the
177   timeframe of nucleogenesis, and point to a role for both type I and type II cadherins in their
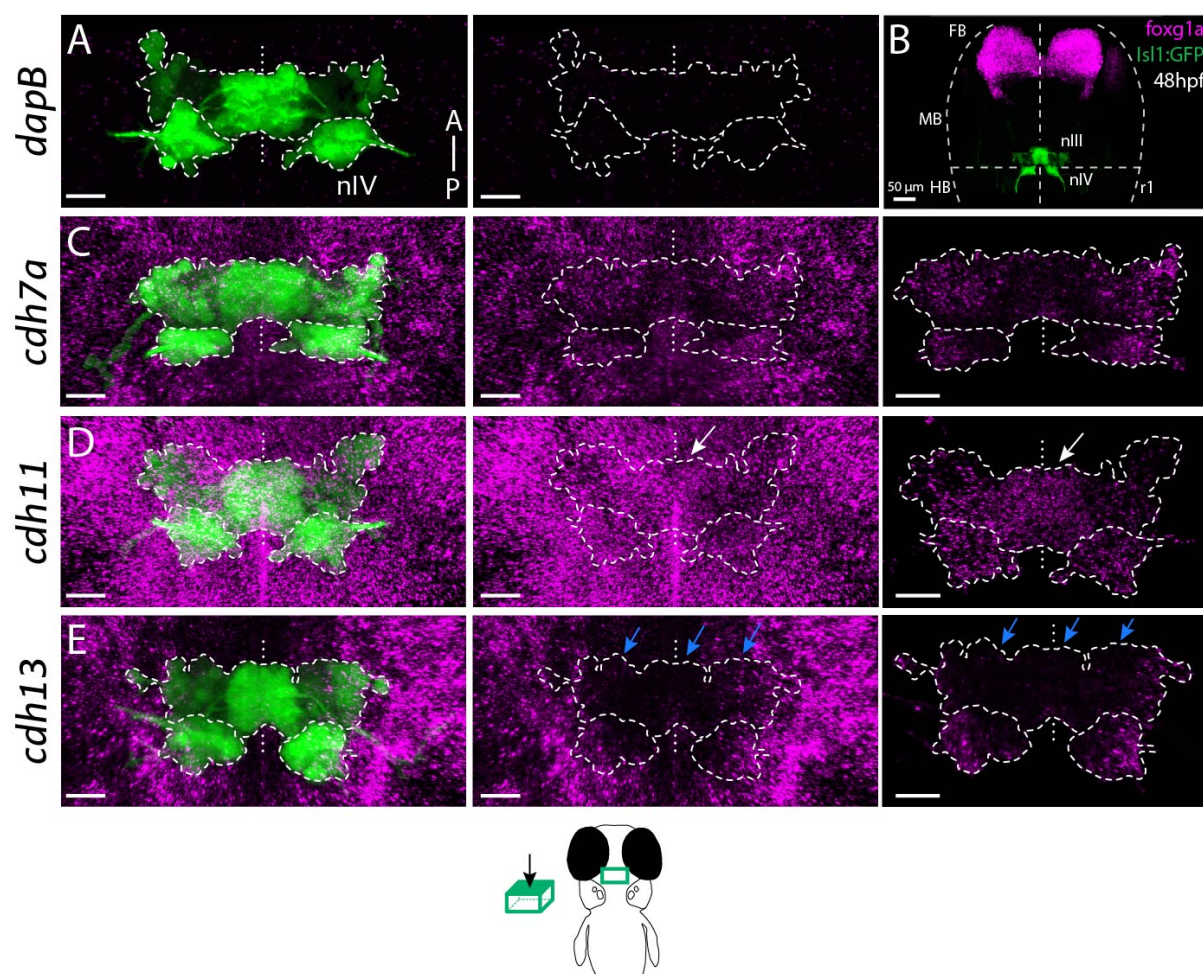178   development.

179

180   Figure 1-figure supplement 1.

181

7

182

183   Figure 1-figure supplement 2.

184

Perturbing cadherin function disrupts clustering of dorsal oculomotor neurons

185

186   As ocular motor neurons express a number of cadherins, we next sought to assay the role

187   of cadherin expression during nucleogenesis by perturbing general cadherin adhesive

188   function in cranial motor neurons in a stable transgenic line, Tg(*isl1:cdh2ΔEC-*

189   *mCherry*)/Tg(*Isl1:GFP*), hereafter referred to as *cdh2ΔEC.* In this line, a dominant negative

190   cadherin construct is expressed under the control of a cranial motor neuron-specific

191   regulatory enhancer of the *Isl1* gene (Rebman et al., 2016). This construct (*cdh2ΔEC*) carries

192   a large deletion encompassing ectodomains 1-4 of *cdh2*, and blocks cadherin adhesive

193   function in an isotype-nonspecific manner, causing non-adhesive phenotypes in cells in

194   which it is overexpressed by occupying sites where endogenous cadherins would otherwise

195   localise, as well as by facilitating their endocytosis (Rebman et al., 2016; Kintner et al., 1992;

196   Nieman et al. 1999; Jontes et al., 2004). As a result, it is expected to perturb both type I and

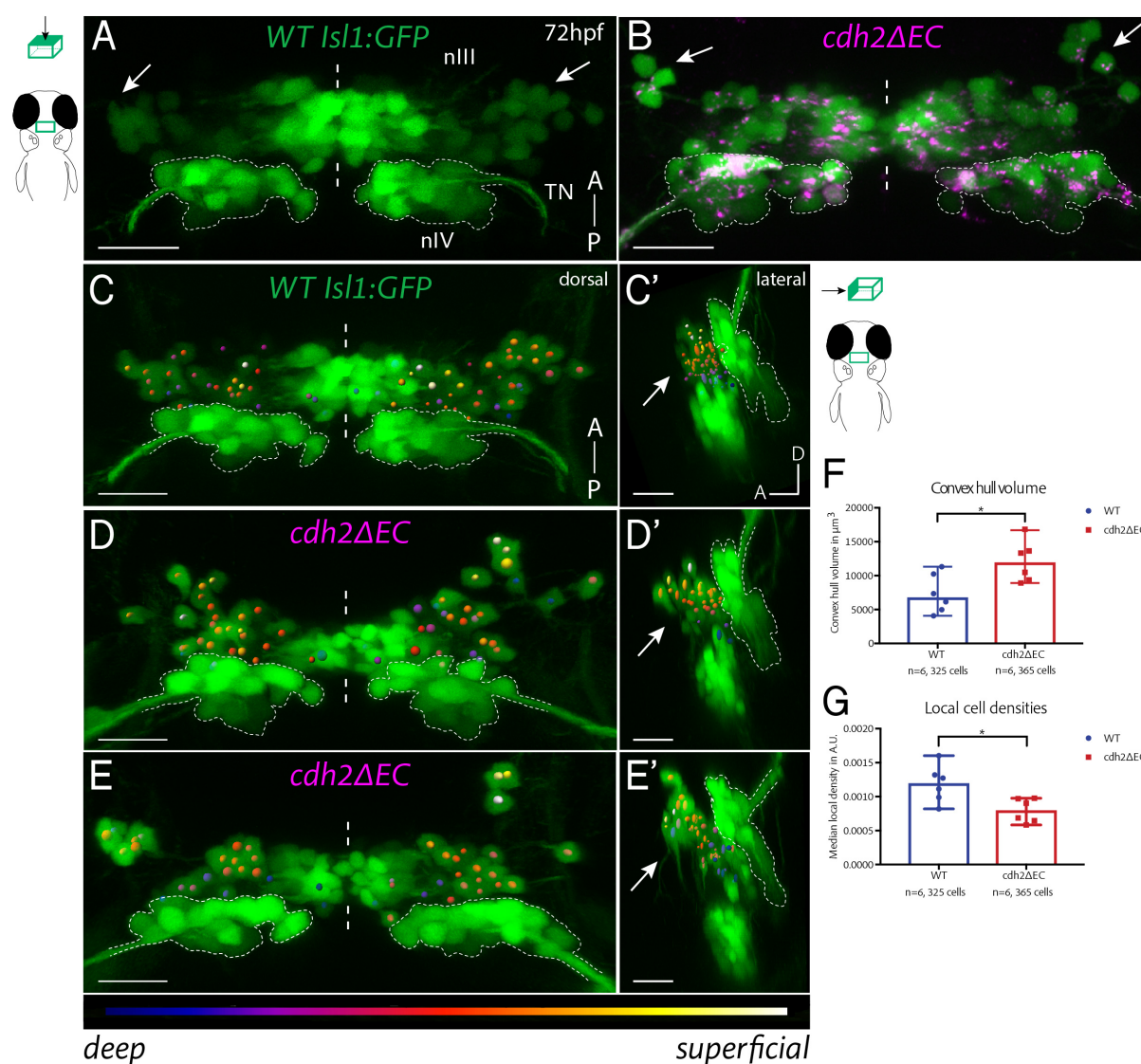197   type II cadherin-mediated adhesion.

199   Figure 2.

200   In order to examine the effect of perturbing cadherin function on the organisation of ocular
201   motor neurons, we performed live imaging of wild-type *Isl1:GFP* and *cdh2ΔEC* larvae at 72
202   hpf (Figure 2), when both nIII and nIV are complete in terms of absolute numbers of terminally
203   differentiated neurons and have also innervated their appropriate muscle targets during
204   normal development. Live imaging revealed expression of *cdh2ΔEC*, as evidenced by
205   punctate mCherry-positive fluorescence, in all GFP-positive nIII neurons, however no signal
206   was observed in adjacent GFP-negative IO neurons, nVI neurons or other surrounding cell
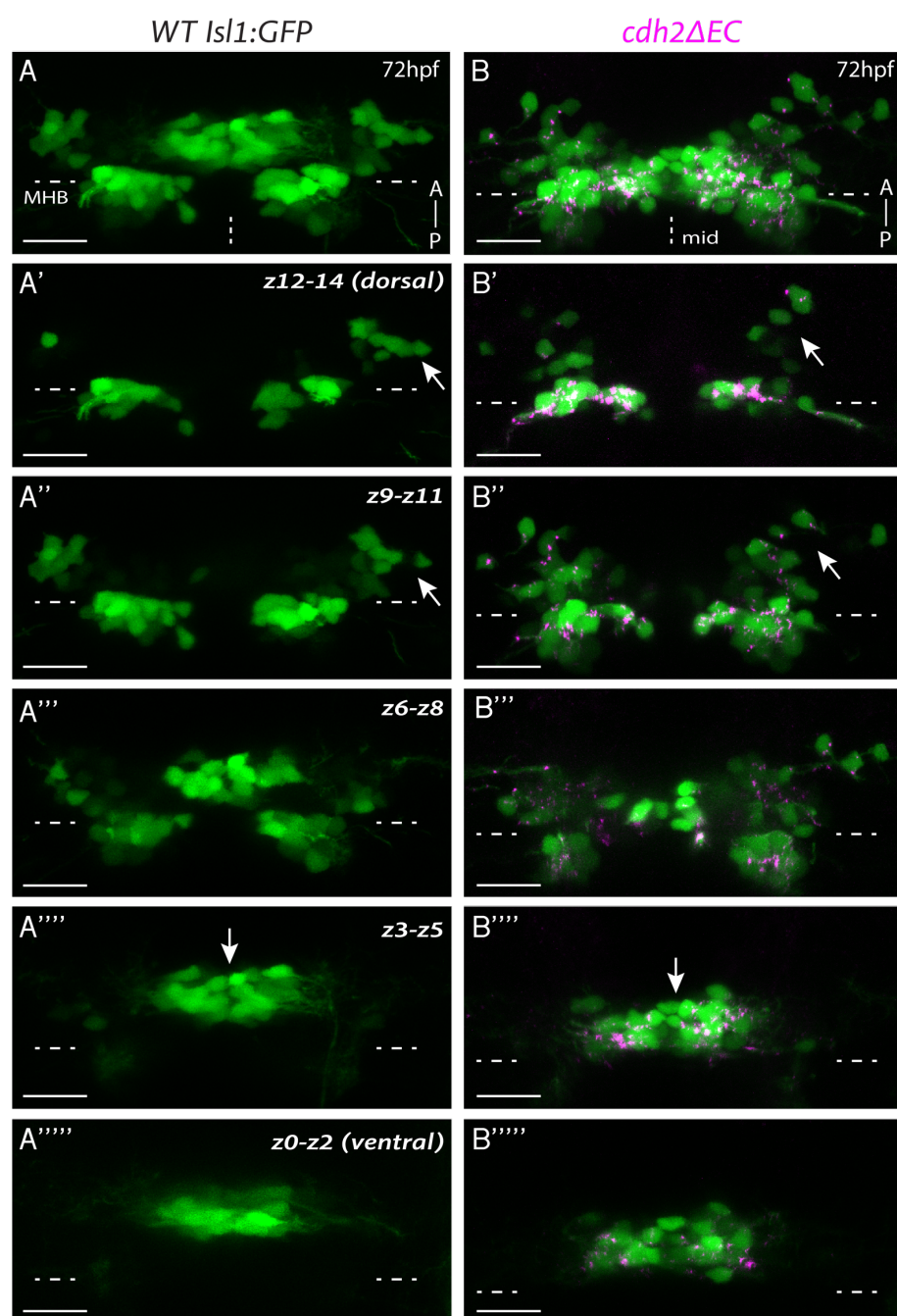207   types, recapitulating the lack of expression observed in *Isl1:GFP* (Figure 2B).

234   Figure 2-figure supplement 1.

235 Following perturbation of cadherin function, dorsal and ventral nIII populations were still
236 visibly distinct as in wild-types (Figure 2-figure supplement 1), however the positioning of
237 dorsal nIII neurons was perturbed (Figure 2B). Two main phenotypes were observed: Firstly,
238 neurons were more sparsely distributed than their wild-type counterparts (Figures 2D-2D').
239 Secondly, they were often also scattered over a wider area, so that occasionally small groups
240 of dorsal cells were found clustered a greater distance away from the rest of the nucleus
241 (Figures 2E-2E'). Interestingly, the density and positioning of neurons located in ventromedial
242 nIII was not perturbed. In order to measure the degree of dispersion, as well as the overall
243 spatial extent of dorsal nIII neurons, three-dimensional cell coordinates were recorded for the
244 dorsal half of nIII (Figures 2C-2E'). The number of cells measured per side, per larva did not
245 differ depending on the genotype (Figure 2G), suggesting that normal programmes of
246 differentiation were unlikely to be affected following perturbation of cadherin function,
247 recapitulating previous findings (Astick et al., 2014). However, there was a significant increase
248 in the convex hull volumes (the volume of the smallest convex set in Euclidean space
249 containing all coordinates) of dorsal nIII neurons in *cdh2ΔEC* larvae (Figure 2F),
250 demonstrating that these neurons occupy a larger area in 3D space as a result of disrupted
251 cadherin function. Furthermore, local cell densities estimated by Delaunay tessellation were
252 significantly reduced in these larvae compared to wild-types (Figure 2G), indicating that,
253 overall, *cdh2ΔEC*-expressing neurons in dorsal nIII have fewer oculomotor neighbours as a
254 result of weakened adhesions. We conclude that cadherins are required for the clustering
255 and correct positioning of IR/MR subnuclei of nIII.

256

257 **Cadherins are required for contralateral migration of ventral superior rectus neurons**
258 In the developing CNS, contralateral connectivity is predominantly established via midline-
259 crossing commissural axons, which are guided by axon guidance factors secreted by midline
260 cells (Ypsilanti et al., 2010). In contrast, the contralateral innervation pattern of superior rectus
261 (SR) neurons, which are located in ventral nIII, is the product of an unusual and well-
262 conserved migration during which they translocate their soma across the midline to the
263 contralateral side (Figure 3A). Studies in other vertebrates have shown that SR neurons send
264 out axons ipsilaterally and migrate to the contralateral side along a leading process which
265 extends into the contralateral nucleus, resulting in contralateral projection (Puelles-Lopez et
266 al., 1975; Bjorke et al., 2016; Dun et al., 2012).
267 In zebrafish, SR neurons which have completed this migration can be detected from 5 dpf
268 (Greaney et al., 2017), however their development has not been fully described in this
269 organism. We initially sought to characterise the time frame of zebrafish SR contralateral

11

270 migration in early development. Using live time-lapse imaging of wild-type *Isl1:GFP* embryos,
271 we identified that bilateral ventral nIII neurons are initially separated at ~43.5 hpf and
272 progressively converge towards the midline, until cells of either side are in contact from ~47
273 hpf. Using immunohistochemistry against GFP in order to examine their arrangement, we
274 found that ventral nIII neurons are found interdigitated at the midline by 72 hpf, suggesting
275 that migration is underway (Figure 3B). We estimate that SR neuron migration is complete by
276 ~4 dpf based on contralateral cells counts following unilateral application of DiI to the orbit
277 of fixed *Isl1:GFP* embryos of various developmental stages, (data not shown).

278 We next asked whether cadherin adhesive function could play a role in regulating SR
279 neuron migration by examining the organisation of ventral nIII neurons at the midline at 50
280 hpf, when midline convergence is usually complete. Whereas wild-type ventral nIII neurons
281 were found fully interdigitated at the midline in the majority of embryos (Figure 3C), only a
282 few *cdh2ΔEC*-expressing neurons had successfully converged, leaving a gap between large
283 numbers of cells (Figure 3D). In order to quantify the degree of midline convergence, we
284 measured the area of GFP fluorescence present in a single sagittal section directly at the
285 midline, obtained from resliced z-stacks (Figures 3E-3G). This was always seen as one large
286 area rather than multiple smaller spots (irrespective of genotype), indicating that cells move
287 towards the midline in a collective fashion. There was a significant decrease in the area of
288 GFP fluorescence imaged in *cdh2ΔEC* embryos (Figure 3F and 3G) compared to wild-types
289 (Figures 3E), whereas no difference was detected in the total numbers of nIII neurons between
290 them. This suggests that convergence of SR neurons towards the midline is perturbed in
291 *cdh2ΔEC* embryos and is unlikely due to delayed neurogenesis. Interestingly, our live imaging
292 experiments at 72 hpf show that *cdh2ΔEC*-expressing SR neurons eventually reach the
293 midline (Figures 2B and 2D-E). Overall these results indicate that perturbing cadherin function
294 delays, but does not prevent, the convergence of SR neurons towards the midline.

295 We next sought to investigate whether cadherin adhesivity regulates later stages of
296 contralateral migration, during which SR neurons cross the midline and migrate into the
297 contralateral nucleus. Using unilateral application of DiI to the oculomotor nerve of fixed
298 larvae at 5 dpf, we labelled groups of contralateral oculomotor neurons in wild-types (Figure
299 3I-3I'), however nIII labelled neurons in *cdh2ΔEC* larvae were only found on the ipsilateral
300 side (Figure 3J-3J'), suggesting that contralateral migration is abolished following loss of
301 cadherin adhesion. In order to examine the distribution of SR neurons in greater detail, we
302 adopted a sparse labelling approach at the same developmental stage. Using unilateral retro-
303 orbital dye fills, oculomotor neurons of *Isl1:GFP* larvae can be traced from their muscle
304 targets and assigned a subnuclear identity based on presence (or absence) of GFP

305   fluorescence and anatomical location (Figure 3H; Greaney et al., 2017). Live imaging revealed

306   dye-filled GFP-positive (SR) cells on the contralateral side in wild-types (Figure 3K-3K''),

307   whereas there was a dramatic reduction in the number of contralateral cells labelled in

308   *cdh2ΔEC* larvae, despite successful labelling of ipsilateral neurons (Figure 3L-L'').

309   Examination of the pooled data revealed a significant relationship between genotype and

310   subnuclear identity (Figure 3M). There was a significant reduction in the proportion of

311   contralateral GFP-positive nIII cells in *cdh2ΔEC* larvae compared to wild-types (Figure 3N),

312   with 15/16 larvae exhibiting proportions of <5% of labelled SR neurons compared with 10/15

313   wild-type larvae, which had proportions of >5% ranging up to 65%. We reasoned that there

314   should be a concomitant increase in the proportions of dye-filled ipsilateral GFP-positive

315   cells, should *cdh2ΔEC* expression have interfered with the ability of SR neurons to migrate.

316   Indeed, there was a significant increase in the proportion of ipsilateral GFP-positive cells in

317   *cdh2ΔEC* larvae (Figure 3O), which likely reflects the additional detection of SR neurons

318   which have failed to migrate to the contralateral side, in addition to IR/MR cells. In contrast,

319   we found no difference in the proportions of dye-filled IO (Figure 3P) or SO/nIV neurons

320   between genotypes (Figure 3Q). Taken together, our results indicate that the contralateral

321   migration of SR neurons depends on cadherin-mediated adhesion. Our finding that SR

322   neurons in which cadherin adhesivity has been perturbed eventually reach the midline, but

323   do not cross it, suggests that contralateral migration proceeds via a two-phase process: an

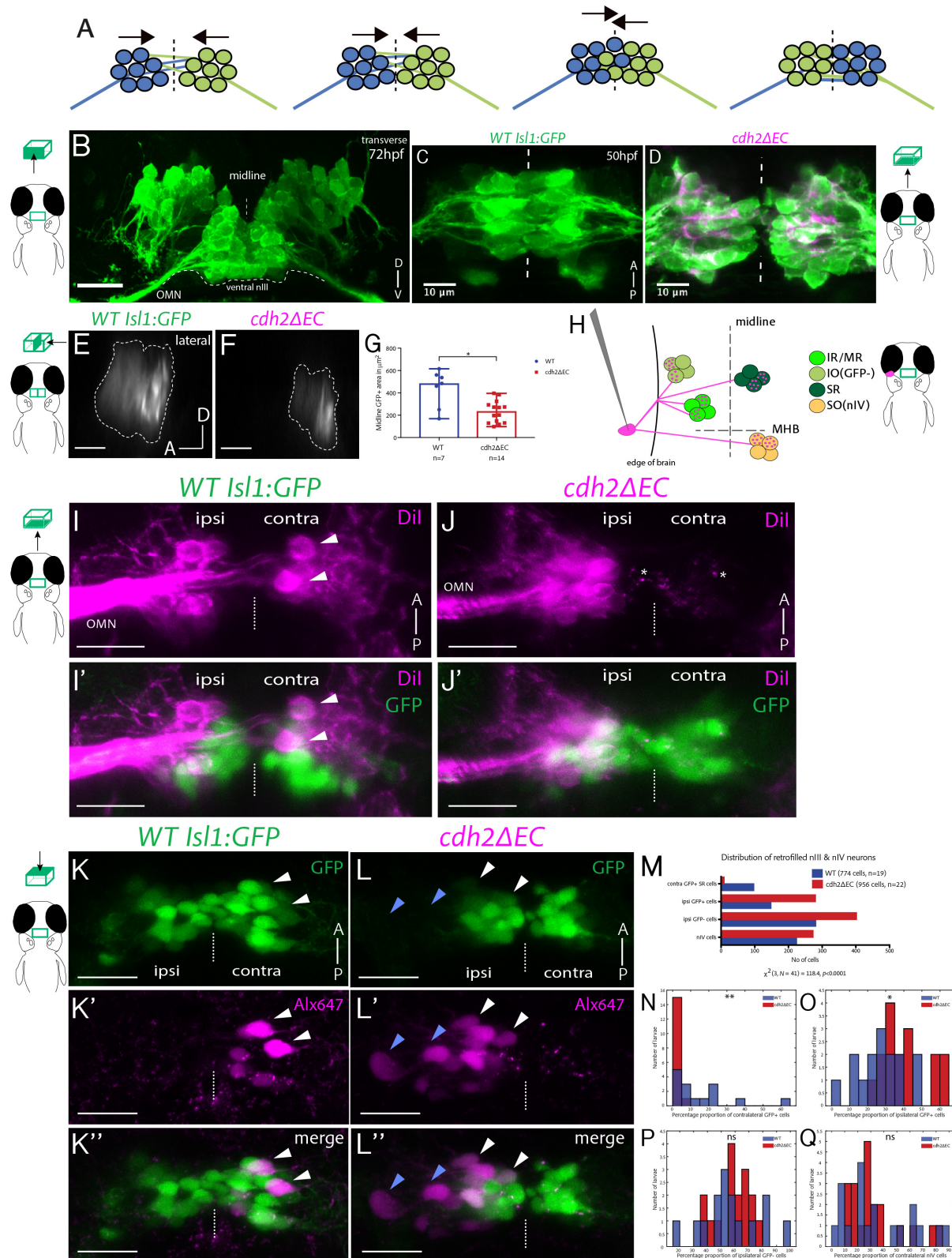324   initial convergence towards the midline, followed by somal translocation across it.

13

325

326   Figure 3.

327

328

Dominant negative cadherin expression results in mispositioning of trochlear neurons along the dorsoventral axis

In addition to nIII, the trochlear nucleus (nIV), which is located proximal to nIII in r1 of the hindbrain is labelled in *Isl1:GFP* fish. To investigate the effect of cadherin perturbation on the positioning of nIV neurons, we performed live imaging at 72 hpf using lateral mounting. Interestingly, although nIV neurons were not scattered, they were aberrantly positioned along the DV axis, resulting in a significantly dorsally elongated trochlear nucleus compared to wild-type fish (Figure 4). The position of nIV did not appear to be shifted overall with respect to nIII. During wild-type development, nIV elongates along the DV axis between 48hpf and 72hpf (unpublished data), suggesting the presence of guidance cues or mechanical forces which act along this axis. We speculate that abrogating cadherin function in these neurons weakens the adhesions which may limit their movement, resulting in increased elongation of the nucleus.
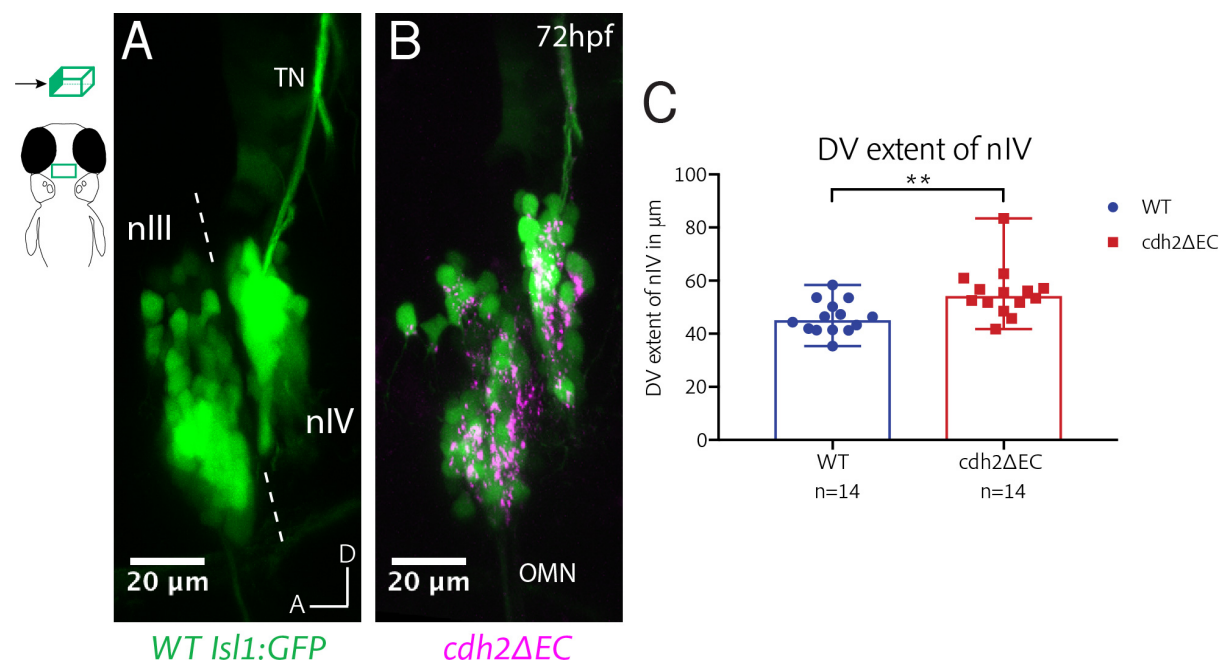

Figure 4.

IO neurons require interactions with neighbouring nIII subpopulations for precise pool positioning

The above experiments identify subpopulation-specific requirements for cadherins in the correct positioning of ocular motor neurons. We next asked whether subnucleus position depends in part on cadherin-based interactions between neurons of different subnuclei, which are spatially proximal. In *cdh2ΔEC* embryos, neurons belonging to the inferior oblique (IO) nucleus were never seen to express *cdh2ΔEC-mCherry*, allowing us to ask whether their position is dependent on cadherin function in other subnuclei. Several cadherins, including *cdh2* and *cdh11*, are expressed by all oculomotor neurons, including IO neurons, whereas other type II cadherins which are capable of interacting heterophilically with *cdh11,* such as *cdh8*, are expressed differentially by subnuclei (Figure 1B-C; Brasch et al., 2018). This raises the possibility that homophilic and heterophilic cadherin-mediated adhesive interactions could arise between IO neurons and other oculomotor neurons. We sparsely labelled IO neurons using retro-orbital dye fills as above and analysed their distribution according to their dorsoventral (DV; 15 bins) and mediolateral (ML; 4 bins) location. We assigned a coordinate to each dye-filled neuron within an overall grid of 60 bins, corresponding to the full spatial extent of nIII. 3D-visualisation of nIII revealed that the IO subnucleus resembles a columnar organisation along the DV axis, with neurons located ventral and lateral to SR neurons, as well as dorsally and medially (Figure 5A-5A'').

We first assessed differences in the distribution of IO neuron location using a multivariate extension of the Kolmogorov-Smirnov test. This revealed that the overall cellular distribution for IO neurons was significantly different between genotypes (k=0.2427, p<0.0001). In wild-types, probabilities of IO location are biased towards medial locations and are found along the DV axis, with slightly higher probabilities for dorsal regions (Figure 5B). In *cdh2ΔEC* larvae, less dorsal and slightly more lateral probabilities were observed for IO neurons (Figure 5C-5D), however the overall arrangement of IO neurons as a subnucleus appeared similar. In order to estimate the full extent of IO neuron distribution, we used a non-parametric Bayesian approach where the probability of a neuron to be placed in any of the 60 bins in the grid is described as a Dirichlet distribution, which is then estimated by performing statistical inference from the observed data. Estimated DV-ML occupancy distributions confirmed differences in the overall spatial distribution of IO neurons between genotypes (Figure 5E-5G). We investigated the directionality of the shift along the two major axes and found an overall tendency towards higher, dorsal values for DV subdivision in wild-types compared to *cdh2ΔEC* larvae (Figure 5H). Additionally, there was a slight tendency overall to lower, medial values for wild-types (Figure 5I). This demonstrates that overall, the positioning of IO neurons of *cdh2ΔEC* larvae is altered compared to wild-types: IO neurons are located more ventral

389   and lateral, consistent with a shift away from adjacent IR/MR and SR subnuclei (Figure 5J-
390   5K). In sum, these results suggest that cadherin-dependent neuron-neuron adhesive
391   interactions between oculomotor subnuclei also contribute to the appropriate positioning of
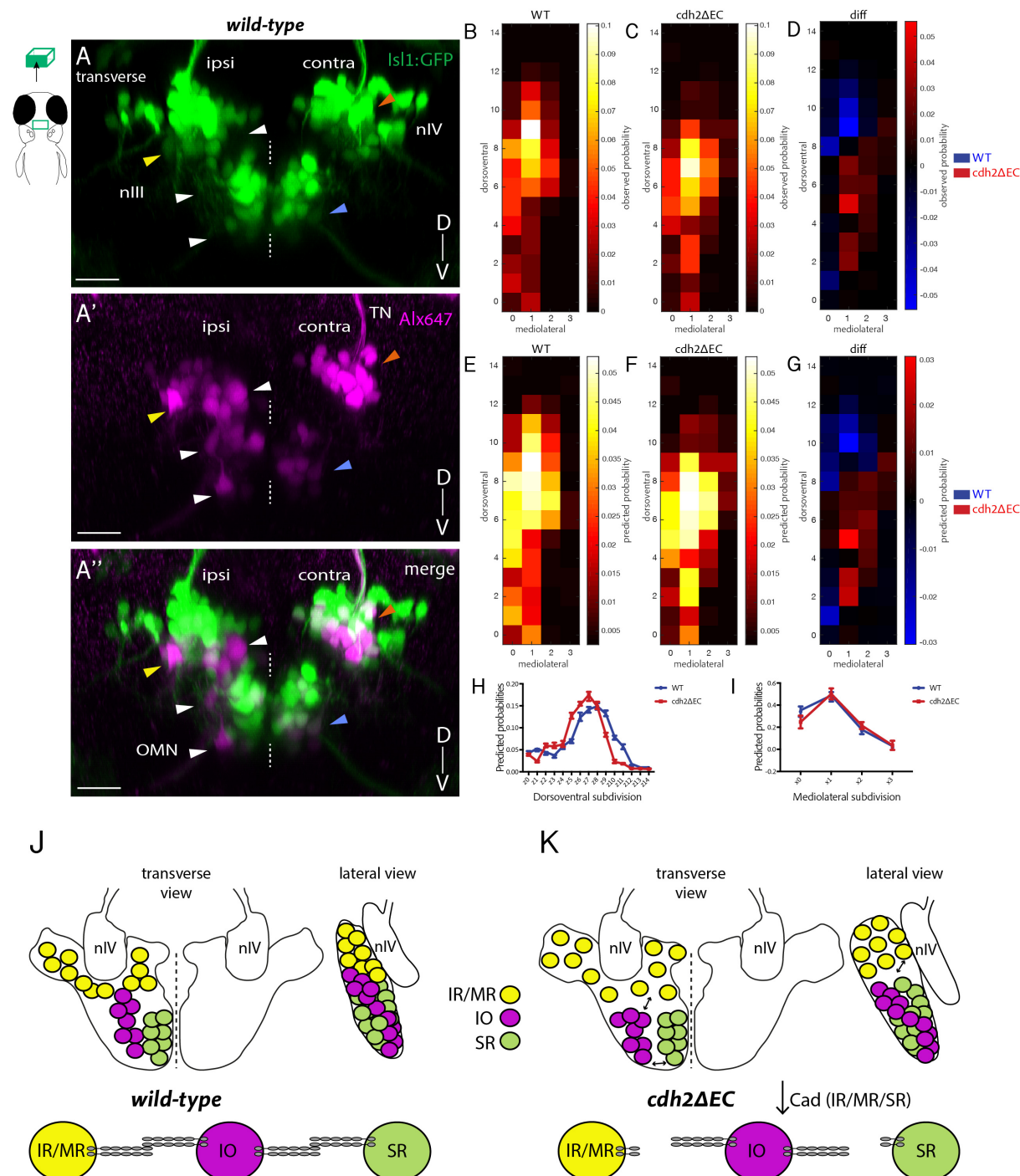392   the IO subnucleus.

393
394   Figure 5.
395
396
397

Neuromuscular connectivity is preserved in *cdh2ΔEC*-expressing ocular motor neurons

Whereas some studies report that perturbations to cadherin signalling in hindbrain cranial motor neurons affect the positioning of soma, while preserving stereotyped patterns of axon outgrowth and pathfinding (Astick et al., 2014; Rebman et al., 2016), others have identified a role for specific classical cadherins in the regulation of normal axonal development in motor neurons, including pathfinding, axon outgrowth and branching (Brusés, 2011; Barnes et al., 2010). To investigate the role of cadherin adhesive function in the development of peripheral ocular motor connectivity, we examined the efferent projections of nIII and nIV neurons in *cdh2ΔEC* larvae using lateral confocal imaging. At 72 hpf, all ocular motor nerves and branches were present and appeared to have reached their respective EOMs (Figure 6A-B). In order to examine possible defasciculation defects, we quantified the number of axon branches belonging to each nerve bundle for each of the four oculomotor nerve (OMN) branches, as well as for the trochlear nerve (TN). There was no significant difference in the number of branches between genotypes (Figure 6C). These observations indicate that axon outgrowth, targeting and fasciculation of ocular motor axons is robust to cell autonomous dominant negative cadherin expression.
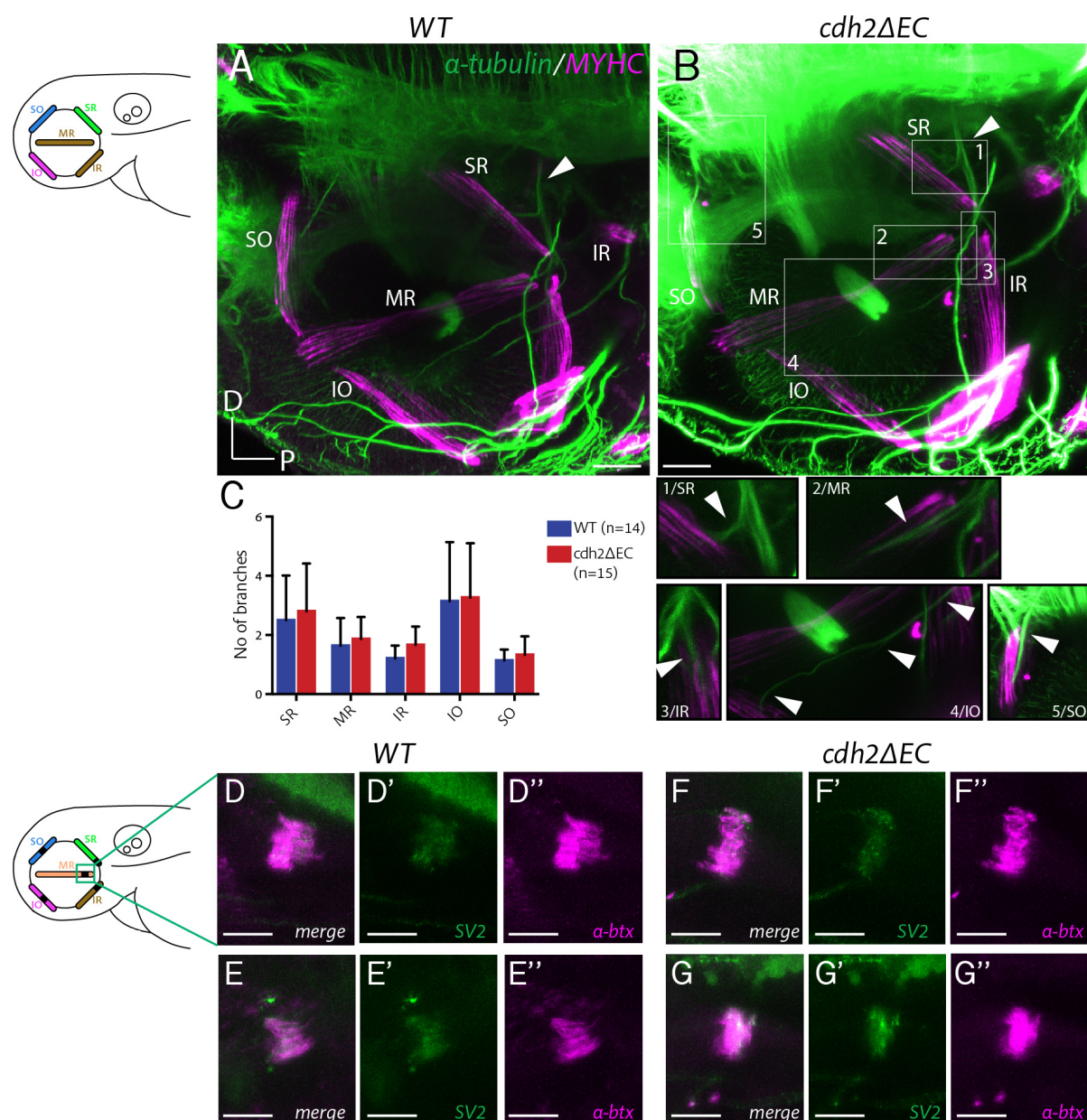
Figure 6.

Once ocular motor axons have navigated to their appropriate targets, initial contacts with the target muscle stabilise and form neuromuscular junctions (NMJs). We have previously shown that synaptogenesis is underway in all muscles from 72 hpf (Clark et al., 2013), correlating with the onset of spontaneous saccadic eye movements (Easter & Nicola, 1997). We next asked whether cadherin function could be required for the formation of NMJs. Cadherins have known roles in the formation of central synapses (reviewed in Salinas & Price, 2011) and cdh2 is known to localise at developing NMJs (Cifuentes-Diaz et al., 1994; Brusés, 2011). We performed immunohistochemistry against the presynaptic vesicle protein SV2 and labelling of postsynaptic acetylcholine receptors using fluorescently tagged α-bungarotoxin

427   at 4 dpf and identified extraocular NMJs according to their spatial location using brightfield

428   signal. We found that pre- and postsynaptic components colocalise as discrete patches on

429   respective EOMs both in wild-types and *cdh2ΔEC* larvae (Figure 6-figure supplement 1A-

430   H''), including on the medial rectus (MR) muscle (Figure 6D-G''), which is one of two muscles

431   driving horizontal eye movements of the larval optokinetic reflex. Furthermore, we observed

432   no difference in the overall area of SV2 signal (Figure 6-figure supplement 1I) or degree of

433   colocalisation (Figure 6-figure supplement 1J), suggesting that NMJs form properly following

434   perturbation of cadherin adhesion. However, we cannot exclude an effect on synapse

435   stabilisation at later stages of development or in the regulation of synaptic strength. Taken

436   together, our findings suggest that perturbing cadherin function does not erode the peripheral

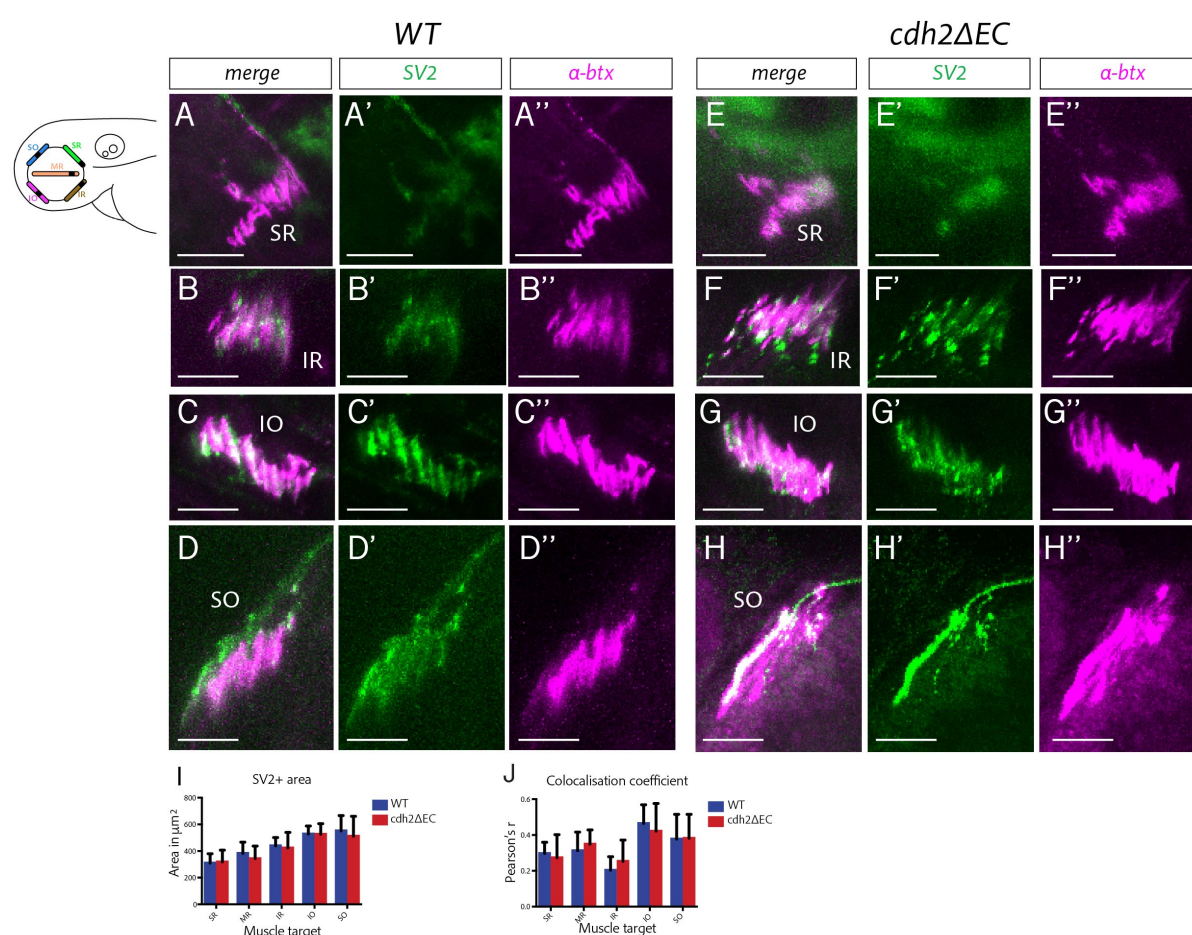437   connection between ocular motor neurons and muscle targets.

438

439   Figure 6-figure supplement 1.

440
441
442

Abrogating cadherin function in developing oculomotor neurons causes eye movement defects

We next considered whether perturbing cadherin-mediated adhesion in oculomotor neurons could impact their emergent motor function by assaying the larval optokinetic reflex (OKR). The OKR is a well-conserved gaze-stabilising reflex which consists of slow-phase and fast reset eye movements in response to optic flow. In zebrafish, the OKR is robust by 3-4 dpf (Easter & Nicola, 1997). We measured the OKR of immobilised zebrafish at 5 dpf by capturing the eye movements of larvae, which were placed within a circular arena, from above with a high-speed video camera as they viewed vertical black and white moving bars of varying speed, contrast and spatial frequency. The horizontal eye movements of the OKR rely on the action of two antagonistic EOMs, the oculomotor-driven medial rectus and abducens nucleus-controlled lateral rectus (Figure 7B). These muscles drive nasal (adduction) and temporal (abduction) eye movements, respectively (Figure 7A-A'). As nVI neurons of *cdh2ΔEC* larvae do not express *cdh2ΔEC*, expression is restricted to MR neurons which are known to be contained within dorsal nIII and display a severely scattered phenotype in *cdh2ΔEC* larvae (Figure 2). We therefore hypothesised that cell-specific perturbation of cadherin function would primarily affect nasal rather than temporal eye movements.

We analysed movement for each individual eye and evaluated the eye gain of the slow-tracking eye movement separately for nasal and temporal movements, as well as eye range. We found that *cdh2ΔEC* larvae displayed severe defects in the efficiency of their nasal eye movements when compared to wild-types (Figure 7C), exhibiting a significant decrease in the eye gain for both eyes across all trials, with the strongest effect seen for the strong eye. Conversely, we found no difference in the eye gain for temporal eye movements between *cdh2ΔEC* larvae and wild-types for either strong or weak eyes (Figure 7D), although variability was higher for *cdh2ΔEC* larvae. We also observed a significant decrease in the eye range of each eye in *cdh2ΔEC* larvae (Figure 7E), with a more pronounced effect observed for the strong eye. Taken together, these data show that the efficiency of nasal eye movements as well as overall range of movement is significantly impaired in larvae in which cadherin-mediated adhesion in oculomotor neurons is reduced. Our finding that the temporal eye movements of the OKR are not impaired is consistent with a specific effect of *cdh2ΔEC* expression on MR-driven motor control rather than visual impairment and suggests that the clustered arrangement of these neurons is important for the function of the motor circuit.
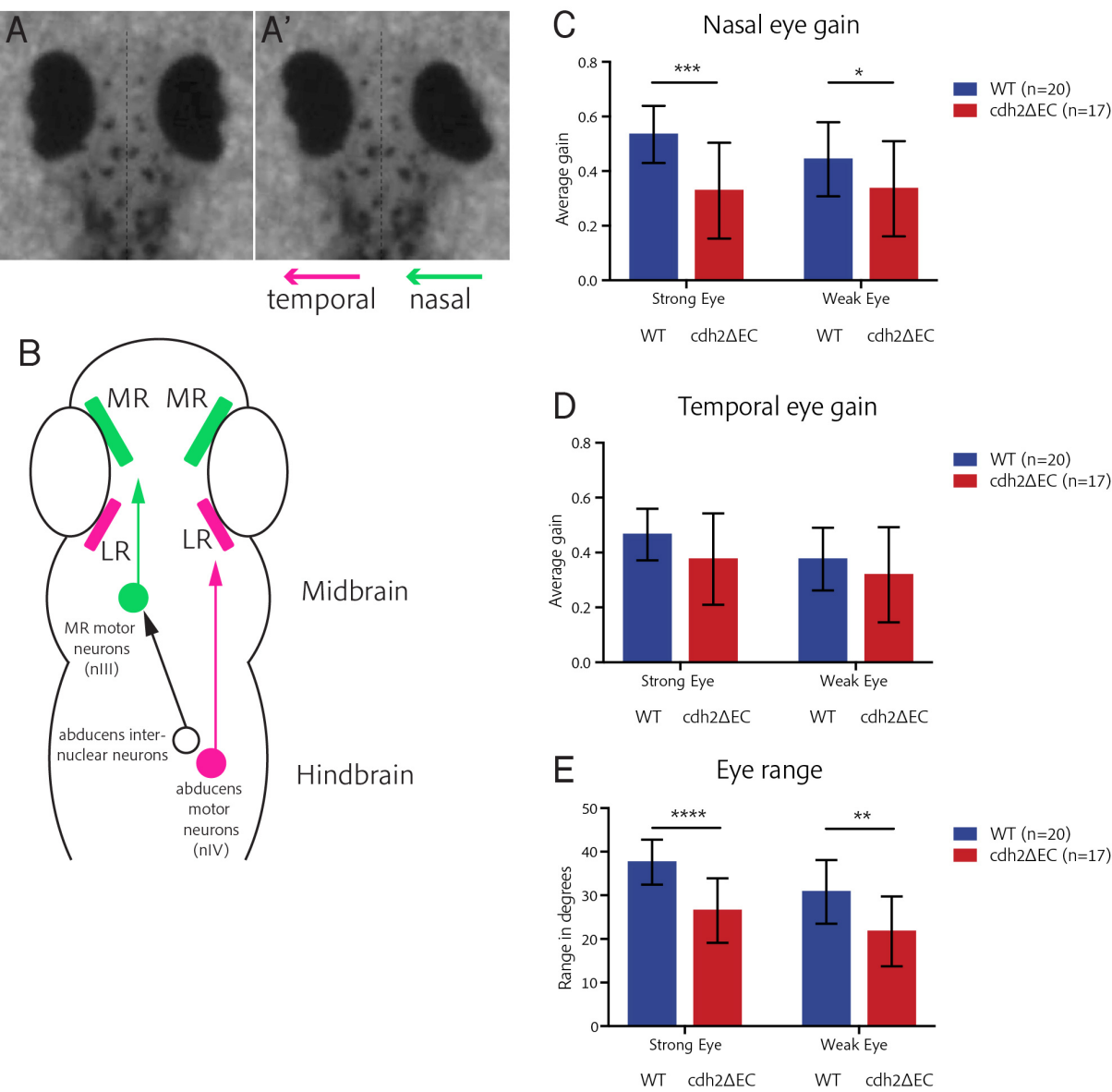
478

479   Figure 7.

480

481

482

483

484

485

486

487

488

489

490

491

Discussion

In this study, we investigated the role of cadherin-mediated adhesion in the development of subnuclear topography, a unique phenomenon whereby clusters of neurons innervating functionally-related muscles via distinct nerve branches further group together, and its affect on motor function. We demonstrate that cadherins control distinct aspects of cranial motor neuron positioning, including the clustering of neurons belonging to dorsal oculomotor subnuclei and contralateral migration of ventral SR neurons, while also regulating subnuclear position through adhesive interactions between constituent oculomotor subnuclei. In addition, we find that eye movements driven by oculomotor neurons in which clustering is perturbed are defective, raising the possibility that their assembly into nuclei is important for circuit function.

Cadherins play roles in the development of specific subnuclei

Our finding that dorsal nIII (IR/MR) and ventral (SR) neurons display differential positioning defects when cadherin function is disrupted in these subnuclei, and that the location of the adjacent IO subnucleus is shifted following this perturbation, shows that cadherin-based interactions coordinate the positioning of motor neurons both *within* and *between* subnuclei. It has previously been proposed that cadherins globally expressed by motor neurons provide a baseline level of adhesion, while selective expression of others facilitates their sorting into distinct nuclei (Demireva et al., 2011). We find that several cadherins, including *cdh2* and *cdh11*, are expressed by all subnuclei, highlighting them as prime candidates to drive baseline levels of adhesion via homophilic interactions. Recent work raises the possibility that heterophilic interactions between members of type II cadherins belonging to specificity groups, such as *cdh8* (expressed to varying degrees by IR/MR and SR) and *cdh11* (expressed by all ocular motor neurons), could also participate, in collaboration with *cdh2* (Brasch et al., 2018; Dewitz et al., 2019).

Whereas we find that that the clustering of dorsal nIII neurons requires cadherin adhesivity, as previously shown for other cranial motor nuclei (Astick et al., 2014), ventral SR neurons do not appear to depend on cadherin function in the same way – here cadherins regulate transmedian migration. Dorsal nIII neurons, which are generated earlier and migrate dorsally, express additional cadherins during development. As such, their coalescence may be more cadherin-dependent. In addition, dorsal subnuclei differentially express several classical cadherins, including *cdh4* and *cdh10a*. In the future, defining the unique transcriptional identities of individual nIII subnuclei in order to manipulate cadherin expression profiles will allow us to uncover the specific roles of these cadherins.

23

Contralateral migration of SR neurons

SR-innervating oculomotor neurons are one of a small number of neuronal cell types known to complete transmedian migration during development (Simon & Lumsden, 1993; Taniguchi et al., 2002). We identify cadherins as one of the few molecular factors regulating this distinctive migration. Our analyses show that they facilitate the timely convergence of SR neurons towards the midline and are required for their subsequent ability to cross it, suggesting that contralateral migration occurs in two steps. Cadherins are known to contribute to cell migration by coupling to retrograde actin flow, thereby acting as a molecular clutch (Bard et al., 2008; Garcia et al., 2015). This constitutes one possible mechanism by which cadherins facilitate the movement of SR neurons across the midline; whether the migration is driven by multiple cadherins or a single cadherin such as *cdh2*, such as in the case of tangential migration of facial branchiomotor neurons (FBMNs), is unknown (Wanner & Prince, 2013; Rebman et al., 2016).

SR migration is underlain by tight spatial and temporal control gated by Slit/Robo-mediated repulsion from the midline (Bjorke et al., 2016), while midbrain dopaminergic neurons have been proposed as a possible source of chemoattractants (Puelles, 1978). Expression of Neuropilins and their class III Semaphorin ligands is dynamic and differential during nIII development, suggesting that the timing of SR migration depends on these cues and receptors (Chilton & Guthrie, 2003). While exact roles are yet to be established experimentally, their dynamic expression could mean that they are downregulated at the time at which migration is usually complete. Delayed convergence by the way of perturbed cadherin-mediated adhesion could therefore affect the ability of SR neurons to respond to guidance cues at the appropriate time. What is the importance of SR contralateral migration for circuit function? The organisation of ocular motor circuitry is highly stereotyped, whereby motor neuron groups controlling coactive muscle pairs on opposite sides of the body are found on the same side of the brain. The failure of SR neurons to complete contralateral migration is likely to be detrimental to motor function, as contralateral innervation of the SR muscle is key to the vertical eye movements of the gaze-stabilising vestibulo-ocular reflex (VOR; Schoppik et al., 2017).

Role of cadherins in development of motor circuit function

Our data show that although the nasal OKR is significantly perturbed when cadherin-mediated adhesion is reduced, the peripheral connection between motor neuron and muscle is left intact, suggesting that these deficits arise as a result of impaired central connectivity of dorsal MR neurons, which fail to coalesce. How might the stereotyped positioning of MR

562   neurons driven by cadherins serve circuit function? MR neurons receive inputs from
563   abducens internuclear neurons (Cabrera et al., 1991), which coordinate conjugate eye
564   movements and could plausibly rely on correct MR neuron positioning for targeting. It would
565   therefore be interesting to test whether these inputs are altered following cadherin
566   perturbations. Previous studies indicate that somal positioning is crucial for arriving sensory
567   afferents: in the mammalian spinal cord, clustering and correct positioning of motor neurons
568   along the dorsoventral axis ensures input specificity and correct motor functioning; similar
569   organisational principles also extend to premotor interneurons which segregate along the
570   mediolateral axis according to their antagonistic output (Sürmeli et al., 2011; Tripodi et al.,
571   2011). In contrast, respiratory behaviours driven by zebrafish FBMNs appear to be robust to
572   manipulations that shift their rostrocaudal location but do not otherwise alter their subnuclear
573   topography, suggesting that they still receive inputs despite perturbed positioning (McArthur
574   & Fetcho, 2017). As such, some aspects of positioning may be more important for the
575   acquisition of input than others.

576   In addition to controlling somal location, one further possible mechanism to mediate the
577   effect of cadherins on larval eye movements could relate to findings that cadherin-dependent
578   clustering of motor neurons underlies the development of gap junction coupling and
579   spontaneous activity (Montague et al., 2017), both of which are known to contribute to mature
580   activity patterns required for motor control (Warp et al., 2012; Chang et al., 1999; Korn &
581   Bennett, 1975). Cadherins may also contribute to selective molecular recognition between
582   neurons within sensorimotor circuits, indeed type II cadherin expression has been shown to
583   delineate functional circuits and control diverse cellular interactions throughout the CNS
584   (reviewed in Redies et al., 2000 and Basu et al., 2015; Friedman et al., 2015; Duan et al.,
585   2018). Circuit function may therefore depend on classical cadherins both for the coordination
586   of cell body positioning, placing critical spatial constraints on connectivity between pre- and
587   postsynaptic partners, and for specificity at the level of individual synapses.

588

589   **Importance of subnuclear topography**

590   Our data show that cadherin-based interactions between subnuclei control the global
591   positioning of a single oculomotor subnucleus, in addition to those which drive the precise
592   positioning of neurons within individual subnuclei. What is the advantage of subnuclear
593   topography? In the mammalian spinal cord, the layout of somatic motor neurons adheres to
594   a higher-order spatial plan, whereby pools innervating functionally related limb muscles are
595   further grouped into columns along the dorsoventral axis (Romanes, 1964; Vanderhorst &
596   Holtstege, 1997). An analogous organisational hierarchy may be present in the brainstem,

25

597　where some cranial motor nuclei are composed of adherent subnuclei which innervate

598　muscles with synergistic functions. With the exception of the MR subnucleus, which receives

599　input from abducens internuclear neurons, oculomotor subnuclei innervating related muscle

600　pairs receive inputs from the same population of central vestibular neurons, which in lateral-

601　eyed vertebrates participate either in the torsional upward (IO-SR) or downward (SO-IR) eye

602　movements of the VOR (Bianco et al, 2012; Schoppik et al., 2017). The grouping of these

603　subnuclei may therefore represent an efficient developmental strategy by which functionally-

604　related neuronal populations acquire inputs from interneurons which drive reflex circuits. The

605　multi-layered organisation of motor neurons is therefore likely to have important implications

606　for the development of connectivity. During nucleogenesis, classical cadherins likely

607　temporally and spatially intersect with several other cell adhesive systems in order to give

608　rise to the stereotyped anatomical arrangement of ocular motor subnuclei. Other studies have

609　highlighted roles for protocadherins, as well as nectin-afadin signalling in the positional

610　control of developing motor neurons (Dewitz et al., 2018; Asakawa & Kawakami, 2019). Our

611　analyses reveal the complexity of motor neuron positioning programmes regulated by a

612　single molecular family within a functional motor circuit. The precise anatomy, robust function

613　and tractability of the zebrafish ocular motor system make it uniquely suited for further

614　investigations into the structure-function relationships underlying circuit formation.

615

616

617

618

619

620

621

622

623

624

625

626

627

628

629

630

631

26

Materials and Methods

Experimental model and transgenic lines

Zebrafish were maintained at 28.5°C on a 14/10h light/dark cycle. Embryos were collected after timed matings and raised in Danieau solution. Staging was performed according to hours post fertilisation (hpf) as previously described (Kimmel et al., 1995). With the exception of behavioural experiments, 0.003% phenylthiourea was added at 24hpf in order to prevent pigment formation. Wild-type, *Tg(Isl1:GFP)* (Higashijima et al., 2000; ZFIN Cat# ZDB-GENO-070810-2, RRID:ZFIN_ZDB-GENO-070810-2) and homozygous *Tg(isl1:cdh2ΔEC-mCherry)vc25/Tg(Isl1:GFP)* (Rebman et al., 2016) zebrafish strains were used in the present study. The latest developmental time point examined was at 5 days post fertilisation (dpf), at which time the sex of individual larvae has not yet been determined. All procedures received Home Office approval and were reviewed by the local Ethics Committee.

Immunohistochemistry

Antibody labeling was performed on whole-mount embryos as previously described (Hunter et al., 2011). Following fixation, embryos were treated with 0.25% trypsin in phosphate-buffered saline (PBS) for 2 minutes at 50 hpf and 3 minutes at 72 hpf and 4 dpf. To label ocular motor neurons at 50 hpf, the CNS was dissected. For synaptic component labelling, larvae were fixed in 4% paraformaldehyde (PFA) for 2 hours and permeabilised using 0.25% trypsin in PBS for 25 mins at room temperature (RT). Larvae were then bisected and incubated in primary antibody solution in PBS-Triton 2% and 1% dimethyl sulfoxide (DMSO) for 2 days at 4°C. The following antibodies were used: anti-GFP 1:500 (Abcam; RRID:AB_300798), anti-RFP 1:200 (MBL Life Science; RRID:AB_591279); anti-acetylated tubulin 1:1000 (Cell Signalling Technologies; RRID:AB_10544694); anti-myosin heavy chain 1:200 (Developmental Studies Hybridoma Bank (DSHB), University of Iowa; RRID:AB_528356); anti-SV2A 1:200 (DSHB; RRID:AB_2315387). Acetylcholine receptors of post-synaptic compartments were stained using a tetramethylrhodamine-α-bungarotoxin conjugate 1:1000 (Invitrogen; RRID: AB_2313931).

RNAscope in situ hybridisation

For detection of mRNA species, RNAscope in situ hybridisation was performed as previously described using an RNAscope Fluorescent Multiplex Reagent kit (320850; ACD, Hayward, CA, USA) using custom-designed probes, with some modifications made to the length of fixation and probe hybridisation and the washing reagent used, as follows (Gross-Thebing et al., 2014): Whole embryos were fixed for 6 hrs at RT in 4% PFA. For larvae fixed at 72 hpf,

666 the CNS was dissected following fixation. 1x RNAscope wash buffer (310091; ACD, Hayward,

667 CA, USA) in ddH$_2$0 was used for all wash steps. Probe hybridisation was performed at 45°C

668 for 22 hrs to ensure full tissue penetration. The following probes were tested: *cdh2, cdh4,*

669 *cdh7a, cdh8, cdh10a, cdh11, cdh13*, as well as *foxg1a* as a positive control and *dapB* as a

670 negative control. Each probe was tested in a minimum of three independent embryos.

Retro-orbital dye fills

672 For DiI fills, embryos or larvae were fixed at relevant developmental stages in 4% PFA at 2hrs

673 at RT, or overnight at 4°C. Specimens were then carefully placed in a small petri dish with a

674 sylgard-coated bottom containing PBS and secured with the eye facing up using a Tungsten

675 minuten pin. The eye was carefully removed from the orbit with sharp forceps and DiI (D3911,

676 Invitrogen) was applied to the tissue at the corner of the orbit, where the oculomotor and

677 trochlear nerves enter, using a blunt microinjection needle held by a micromanipulator. DiI

678 was left to bind to the tissue for 3-5 minutes, after which embryos were stored overnight in

679 PBS at 4°C. The following day, brains were dissected from whole larvae and mounted for

680 imaging. For live retro-orbital dye fills, ocular motor nuclei were retrogradely labelled as

681 previously described (Greaney et al., 2017). Crystallised fluorescently-conjugated Alexa Fluor

682 647 dye (10,000 molecular weight, Thermo Fisher D-22914) was applied unilaterally to the

683 orbit of anesthetised fish at 4 dpf and the side of incision and dye application was recorded

684 for each larva. Larvae were returned to the incubator at 28.5°C to recover overnight before

685 imaging at 5 dpf.

686

Identification of retro-orbital dye-filled neurons as specific ocular motor neurons

688 In wild-type larvae, dye-filled neurons can be assigned to specific extraocular muscles

689 (EOMs) based on the lack of GFP expression in the IO-innervating population in the

690 *Tg(isl1:GFP)* line (Higashijima et al., 2000; Greaney et al., 2017), as well as known projection

691 patterns of ocular motor neurons across vertebrates (Evinger, 1988), whereby superior EOMs

692 are innervated by contralateral ocular motor neurons. The SO-innervating nIV is visible as a

693 discrete nucleus separated from nIII by the midbrain-hindbrain boundary (MHB), therefore

694 contralateral dye-filled nIV neurons are easily distinguished from nIII neurons. Contralateral

695 GFP-positive neurons belonging to nIII are therefore classified as SR neurons. Dye-filled

696 ipsilateral neurons are therefore assigned based on presence or absence of GFP

697 fluorescence: GFP-negative neurons belong to the IO subnucleus, whereas GFP-positive

698 neurons are IR/MR neurons.

699

700

701 *Microscopy and image analysis*

702 For all *in vivo* and *ex vivo* preparations, embryos were mounted in 1% low-melting point (LMP)
703 agarose and imaging was performed on a Zeiss LSM880 Laser Scanning confocal
704 microscope with a 20x (NA 0.95) water-immersion objective. All images were acquired as z-
705 stacks with optical sections spaced at 1μm. For image analysis, Fiji/Image J
706 (RRID:SCR_002285) and Imaris 9 (Bitplane; RRID:SCR_007370) software was used.

707

708 *Analysis of dorsal oculomotor neuron clustering*

709 Dorsal oculomotor neurons were defined as neurons located in the dorsal half of the
710 oculomotor nucleus as ascertained by finding the first and last optical section in the z-stack.
711 Neurons were recorded using the Imaris 9 (Bitplane) Spots Detection tool using parameters
712 optimised for detection of 3-dimensional centre coordinates ~6μm across and manual
713 curation. Coordinates were measured for each nucleus on either side of the midline for each
714 larva. Measures derived from these coordinates were averaged within each larva to provide
715 one value for each specimen. Delaunay tessellations were applied to the coordinates using a
716 custom written MATLAB script (RRID:SCR_001622) to provide estimates of local cell
717 densities, code available on GitHub (https://github.com/aknufer/MN_delaunay).

718

719 *Image analysis of dye-filled neurons*

720 In order to prevent bleed-through of Alexa 647 fluorescent signal into the 488nm channel,
721 control dye-filled larvae without GFP fluorescence and GFP-positive larvae without dye-fills
722 were imaged in order to establish appropriate imaging parameters. Motor neuron identity was
723 assigned using simultaneous visualisation of confocal z-stacks in Imaris 9 (Bitplane) and
724 Fiji/Image J and cells were only counted which revealed a smooth distribution of dextran
725 labelling. Cell locations were recorded using the Cell Counter functionality in Fiji/Image J (Kurt
726 de Vos, University of Sheffield) while 3D-visualisation in Imaris 9 (Bitplane) was employed to
727 distinguish between GFP-positive and -negative cells. The use of interactive 3D-visualisation
728 in Imaris 9 offered considerable advantages to 2D-visualisation when distinguishing dimly
729 fluorescent GFP-positive, dye-filled neurons from GFP-negative, dye-filled neurons.
730 Adjustments to brightness and contrast using the Imaris Display Adjustment function revealed
731 that the former possessed cell-shaped GFP signal which could be visualised from different
732 angles, while the latter had no or only unstructured and noisy contaminating GFP signal from
733 adjacent neurons.

734

735

736 *Analysis of spatial distribution of IO cells*

737 Confocal z-stacks were split into 15 and four equally spaced dorsoventral (DV) and

738 mediolateral (ML) subdivisions (*z0* to *z14*, ventral to dorsal; *x0* to *x3*, medial to lateral) per

739 larva. This was based on the first and last GFP- or Alx647-positive nIII cell for DV subdivisions

740 and on the distance between the lateral most nIII cell and the midline for ML subdivisions.

741 Each ipsilateral GFP-negative dye-filled neuron was assigned a DV and ML coordinate based

742 on location. We adopted a Bayesian approach to provide a non-parametric characterisation

743 of the spatial distribution of IO neurons. We attributed an occupancy probability to each of the

744 K = 15 x 4 mutually exclusive bins across DV and ML axes. Occupancy probabilities were

745 modeled by a Dirichlet distribution with corresponding parameters estimated from the

746 observed data using statistical inference. We used custom R scripts employing the JAGS

747 library (RRID:SCR_017573) to draw 20,000 Markov Chain Monte Carlo (MCMC) samples

748 from the posterior distribution of the occupation probabilities, code available on GitHub

749 (https://github.com/giovannidiana/MN_topo). This method allowed us to estimate average

750 occupancy distributions as well as confidence intervals. To examine the overall difference

751 between the posterior distributions of IO neuron location between genotypes, we estimated

752 the Kullback-Leibler (KL) divergence between their occupancy distributions across the MCMC

753 samples. To choose a sufficient number of posterior samples we used the stability of the

754 posterior *KL* distribution as convergence criterion. The directionality of shifts in IO location

755 between genotypes along DV (*z-shift*) and ML (*x-shift*) axes was computed by calculating the

756 difference between the average DV and ML positions from the occupancy probabilities of each

757 genotype (e.g. *z_shift = z_shift_wt − z_shift_cdh2ΔEC)*.

758

759 *Analysis of axon pathways and neuromuscular junctions*

760 For analysis of ocular motor axons, FIJI cell counter plugin was used to manually count

761 numbers of axon branches for each target muscle in confocal z-stacks. Branches were

762 counted within a 50μm x 50μm window. All branches were counted if they (a) innervated a

763 target muscle or (b) emerged as secondary processes from a branch innervating a target

764 muscle. Branch width was not considered. For analysis of NMJs, synaptic sites were

765 identified based on their anatomical location in the orbit using brightfield signal.

766 Colocalisation of pre-synaptic and post-synaptic components was performed on ROIs of

767 substacks taken from larger confocal z-stacks.

768

769

770

Optokinetic reflex (OKR) assay and analysis

Horizontal eye movements were assayed at 5 dpf using a custom-built apparatus similar in design to Brockerhoff (2006) and controlled using custom LabView (National Instruments, RRID:SCR_014325) routines. Larvae were mounted singly in a small drop of 2% LMP agarose (A9414, Sigma) with the dorsal side up, in the middle of a 35mm non-treated petri dish, to which 1x Danieau solution was added. For OKR recordings, we used a projector (AAXA P2 Jr) and a cold mirror (Thorlabs) to project vertical stripes onto a cylindrical screen. Larvae were positioned in the centre of this screen. A 850 nm LED array illuminated the fish from below. Imaging was performed at 100 Hz using a camera (Thorlabs) fitted with a machine vision lens and a filter (R72 52mm HOYA) to block visible light. Each larva was presented with a horizontally moving vertical grating of varying stimulus parameters, including varying speeds, spatial frequency and contrast using Psychophysics Toolbox (Brainard, 1997). Gratings reversed direction every 6 seconds. Eye position was tracked online by thresholding images and computing the central moments of the two largest binary objects, which invariably corresponded to the eyes. The gain of OKR slow-phase movements was quantified separately for left and right eyes as well as for nasal and temporal directions, as the ratio of eye velocity to grating velocity (custom MATLAB scripts). The range of eye movement (from the resting position of the eye towards rostral or caudal positions in degrees) was evaluated as the maximum/minimum position for each eye. Strong and weak eyes for each larva were assigned based on the eye displaying the greatest eye range.

Quantification and Statistical Analysis

All standard statistical analyses were performed in Prism7 (Graphpad; RRID:SCR_002798) or MATLAB. For normally distributed data, parametric tests were used to make statistical comparisons between groups. For one or more independent groups, Welch's t-tests (with the Holm-Sidak method for multiple comparisons, where applicable) were used. For non-normally distributed data, non-parametric tests were used to make statistical comparisons between groups. For two independent groups, the Mann-Whitney U test was used. For multidimensional data, a multivariate extension of the Kolmogorov-Smirnov test was applied. In order to assess differences between experimental conditions with categorical outcomes, chi-squared-tests were used. Bayesian statistics were applied to perform non-parametric estimation of the spatial organisation of IO neurons. Wherever possible, analyses were performed blind. For behavioural experiments, the number of experimental animals per group was chosen to approximate or slightly exceed that of previously published studies employing a similar experimental design (Schoonheim et al., 2010; Bianco et al., 2012).

Acknowledgements

Competing interests

The authors declare no competing interests.

References

851   **References**

852

853   Asakawa, K. & Kawakami, K. (2018). Protocadherin-Mediated Cell Repulsion Controls the Central
854   Topography and Efferent Projections of the Abducens Nucleus. Cell Reports *24*, 1562-1572.

855   Astick, M., Tubby, K., Mubarak, W. M., Guthrie, S. & Price, S. R. (2014). Central topography of cranial
856   motor nuclei controlled by differential cadherin expression. Current Biology *24*, 1-7.

857   Bard, L., Boscher, C., Lambert, M., Mège, R-M., Choquet, D & Thoumine, O. (2008). A Molecular
858   Clutch between the Actin Flow and N-Cadherin Adhesions Drives Growth Cone Migration. The
859   Journal of Neuroscience *28*(23), 5879-5890.

860   Barnes, S., Price, S., Wentzel, C., & Guthrie, S. (2010). Cadherin-7 and cadherin-6B differentially
861   regulate the growth, branching and guidance of cranial motor axons. Development *137*(5), 805–814.

862   Basu, R., Taylor, M. R. & Williams, M. E. (2015). The classic cadherins in synaptic specificity. Cell
863   Adhesion and Migration *9*(3), 193-201.

864   Bianco, I. H., Ma, L-H., Schoppik, D., Robson, D. N., Orger, M. B., Beck, J. C., Li, J. M., Schier, A. F.,
865   Engert, F. & Baker, R (2012). The Tangential Nucleus Controls a Gravito-inertial Vestibulo-ocular
866   reflex, *22*(14), 1285-1295.

867   Bjorke, B., Shoja-Taheri, F., Kim, M., Robinson, G. E., Fontelonga, T., Kim, K-T., Song, M-R &
868   Mastick, G. S. (2016). Contralateral migration of oculomotor neurons is regulated by Slit/Robo
869   signaling. Neural Development *11*(18), 1-17.

870   Brainard, D. H. (1997). The Psychophysics Toolbox. Spatial Vision *10*(4), 433-436.

871   Brasch, J, Katsamba, P. S., Harrison, O. J., Troyanovsky, S., Honig, B. & Shapiro, L. (2018).
872   Homophilic and Heterophilic Interactions of Type II Cadherins Identify Specificity Groups Underlying
873   Cell-Adhesive Behavior. Cell Reports *23*, 1840-1852.

874   Brockerhoff, S. (2006). Measuring the optokinetic response of zebrafish larvae. Nature Protocols *1*(5),
875   2448- 2451.

876   Brusés. (2011). N-cadherin regulates primary motor axon growth and branching during zebrafish
877   embryonic development. Journal of Comparative Neurology *519*, 1797-1814.

878   Cabrera, B., Torres, B., Pásarao, R., Pastor, A. M. & Delgado-García, J. M. (1991). A Morphological
879   Study of Abducens Nucleus Motoneurons and Internuclear Neurons in the Goldfish (Carrassius
880   auratus). Brain Research Bulletin *28*, 137-144.

881   Chang, Q., Gonzalez, M. & Pinter, M. J. (1999). Gap junctional coupling and patterns of connexin
882   expression among neonatal rat lumbar spinal motor neurons. The Journal of Neuroscience *19*(24),
883   10813-10828.

884   Chilton, J. K. & Guthrie, S. (2003). Cranial Expression of Class 3 Secreted Semaphorins and Their
885   Neuropilin Receptors. Developmental Dynamics *228*, 726-733.

886   Cifuentes-Diaz, C., Nicolet, M., Goudou, D., Rieger, F. & Mege, R. M. (1994). N-cadherin expression
887   in developing, adult and denervated chicken neuromuscular system: accumulations at both the
888   neuromuscular junction and the node of Ranvier. Development *120*, 1-11.

889 Clark, C., Austen, O., Poparic, I. & Guthrie, S. (2013). α2-Chimaerin Regulates a Key Axon Guidance
890 Transition during Development of the Oculomotor Projection. The Journal of Neuroscience *33*(42),
891 16540- 16551.

892 Danesin, C., Peres, J., Johansson, M., Snowden, V., Cording, A., Papalopulu, N., & Houart, C.
893 (2009). Integration of Telencephalic Wnt and Hedgehog Signaling Center Activities by Foxg1.
894 Developmental Cell *16*(4), 576–587.

895 Demireva, E. Y., Shapiro, L. S., Jessell, T. M. & Zampieri, N. (2011). Motor Neuron Position and
896 Topographic Order Imposed by b- and g-catenin Activities. Cell *147*(3), 641-652.

897 Dewitz, C., Pimpinella, S., Hackel, P., Akalin, A., Jessell, T. M. & Zampieri, N. (2018). Nuclear
898 organization in the spinal cord depends on motor neuron lamination orchestrated by catenin and
899 afadin function. Cell Reports *22*(7), 1681-1694.

900 Dewitz, C., Duan, X. & Zampieri, N. (2019). Organization of motor pools depends on the combined
901 function of N-cadherin and type II cadherins. Development *146*, dev180422.

902 Duan, X., Krishnaswamy, A., Laboulaye, M. A., Liu, J., Peng, Y-R., Yamagat, M., Toma, K. & Sanes,
903 J. R. (2018). Cadherin Combinations Recruit Dendrites of Distinct Retinal Neurons to a Shared
904 Interneuronal Scaffold. Neuron *99*(6), 1145-1154.

905 Dun, X-P., Bandeira de Lima, T., Allen, J., Geraldo, S., Gordon-Weeks, P. & Chilton, J. K. (2012).
906 Drebrin controls neuronal migration through the formation and alignment of the leading process.
907 Molecular and Cellular Neuroscience *49*, 341-350.

908 Easter, S. S. & Nicola, G. N. (1997). The Development of Eye Movements in the Zebrafish *(Danio*
909 *rerio)*. Development of Eye Movements, 267-276.

910 Evinger, C. (1988). Extraocular motor nuclei: location, morphology and afferents. In: Büttner-Ennever,
911 J. A. (Ed.), Neuroanatomy of the Oculomotor System. Elsevier, Amsterdam, pp. 81-117.

912 Friedman, L. G., Riemslagh, F. W., Sullivan, J. M., Mesias, R., Williams, F. M., Huntley, G. W. &
913 Benson, D. L. (2015). Cadherin-8 expression, synaptic localization and molecular control of neuronal
914 form in prefrontal cortico-striatal circuits. Journal of Comparative Neurology *523*(1), 75-92.

915 Garcia, M., Leduc, C., Lagardėre, M., Argento, A., Sibarita, J-B. & Thoumine, O. (2015). Two-tiered
916 coupling between flowing actin and immobilized N-cadherin/catenin complexes in neuronal growth
917 cones. PNAS, 6998-7002.

918 Gilland, E. & Baker, R. (2005). Evolutionary Patterns of Cranial Nerve Efferent Nuclei in Vertebrates.
919 Brain, Behavior and Evolution *66*, 234-254.

920 Graf, W. & McGurk, J. F. (1985). Peripheral and Central Oculomotor Organization in the Goldfish,
921 *Carassius auratus*. Journal of Comparative Neurology *239*, 391-401.

922 Greaney, M. R., Privorotskiy, A. E, D'Elia, K. P. & Schoppik, D. (2017). Extraocular motoneuron pools
923 develop along a dorsoventral axis in zebrafish, Danio rerio. Journal of Comparative Neurology, 1-14.

924 Gross-Thebing, T., Paksa, A., & Raz, E. (2014). Simultaneous high-resolution detection of multiple
925 transcripts combined with localization of proteins in whole-mount embryos. BMC Biology *12*(1), 55.

926 Hasan, K. B., Agarwala, S. & Ragsdale, C. W. (2010). PHOX2A regulation of oculomotor complex
927 nucleogenesis. Development *137*, 1205-1213.

928   Higashijima, S., Hotta, Y. & Okamoto, H. (2000). Visualization of cranial motor neurons in live
929   transgenic zebrafish expressing green fluorescent protein under the control of the islet-1
930   promoter/enhancer. The Journal of Neuroscience *20*(1), 206-218.

931   Hunter, P. R., Nikolaou, N., Odermatt, B., Williams, P. R., Drescher, U. & Meyer, M. P. (2011).
932   Localization of Cadm2a and Cadm3 Proteins During Development of the Zebrafish Nervous System.
933   The Journal of Comparative Neurology *519*, 2252-2270.

934   Jontes, J. D., Emond, M. R. & Smith, S. J. (2004). In Vivo Trafficking and Targeting of N-Cadherin to
935   Nascent Presynaptic Terminals. The Journal of Neuroscience *24*(41), 9027-9034.

936   Kimmel, C.B., Ballard, W.W., Kimmel, S.R., Ullmann, B., and Schilling, T.F. (1995). Stages of
937   embryonic development of the zebrafish. Developmental Dynamics *203*, 253–310.

938   Kintner, C. (1992). Regulation of embryonic cell adhesion by the cadherin cytoplasmic domain. Cell
939   *69*(2), 225-236.

940   Korn, H., & Bennett, M. V. (1975). Vestibular nystagmus and teleost oculomotor neurons: functions of
941   electrotonic coupling and dendritic impulse initiation. Journal of Neurophysiology *38*(2), 430–51.

942   Landmesser, L., (1978). The distribution of motoneurones supplying chick hind limb muscles. Journal
943   of Physiology *284*, 371-389.

944   Luiten, P. G. M. & Dijkstra-de Vlieger, H. P. (1978). Extraocular Muscle Representation in the
945   Brainstem of the Carp. The Journal of Comparative Neurology *179*, 669-676.

946   McArthur, K. L. & Fetcho, J. R. (2017). Key Features of Structural and Functional Organization of
947   Zebrafish Facial Motor Neurons are Resilient to Disruption of Neuronal Migration. Current Biology *27*,
948   1746-1756.

949   Montague, K., Lowe, A. S., Uzquiano, A. Knüfer, A., Astick, M., Price, S. R. & Guthrie, S. (2017). The
950   assembly of developing motor neurons depends on an interplay between spontaneous activity, type II
951   cadherins and gap junctions. Development *144*, 830-836.

952   Naujoks-Manteuffel, C., Sonntag, R., & Fritzsch, B. (1991). Development of the amphibian oculomotor
953   complex: Evidences for migration of oculomotor motoneurons across the midline. Anatomy and
954   Embryology *183*(6), 545–552.

955   Nieman, M. T., Kim, J-B., Johnson, K. R. & Wheelock, M. J. (1999). Mechanism of extracellular
956   domain- deleted dominant negative cadherins. Journal of Cell Science *112,* 1621-1632.

957   Patel, S. D., Ciatto, C., Chen, C. P., Bahna, F., Rajebhosale, M., Arkus, N., Schieren, I., Jessell, T.
958   M., Honig, B., Price, S. R. & Shapiro, L. (2006). Type II cadherin ectodomain structures: implications
959   for classical cadherin specificity. Cell *124*(6), 1255–68.

960   Price, S. R., Garcia, N. V., Ranscht, B. & Jessel, T. M. (2002). Regulation of motor neuron pool
961   sorting by differential expression of type II cadherins. Cell *109*, 205-216.

962   Puelles, L. (1978). A Golgi-Study of oculomotor neuroblasts migrating across the midline in chick
963   embryos. Anatomy and Embryology *152*(2), 205–215.

964   Puelles-Lopez, L., Malagon-Cobos, F. & Génis-Galvez, J. M. (1975). The migration of oculomotor
965   neuroblasts across the midline in the thick embryo. Experimental Neurology *47*, 459-469.

966 Rebman, J. K., Kirchoff, K. E. & Walsh, G. S. (2016). Cadherin-2 is Required Cell Autonomously for
967 Collective Migration of Facial Branchiomotor Neurons. PLOS One, 1-18.

968 Redies, C. (2000). Cadherins in the central nervous system. Progress in Neurobiology *61*, 611–648.

969 Romanes, G.J. (1964). The motor pools of the spinal cord. Progress in Brain Research *11*, 93–119.

970 Salinas, P. C. & Price, S. R. (2005). Cadherins and catenins in synapse development. Current
971 Opinion in Neurobiology *15*(1), 73-80.

972 Schoppik, D., Bianco, I. H., Prober, D. A., Douglass, A. D., Robson, D. N., Li, J., Greenwood, J.,
973 Soucy, E. & Engert, F. (2017). Gaze-Stabilizing Central Vestibular Neurons Project Asymmetrically to
974 Extraocular Motoneuron Pools. The Journal of Neuroscience *37*(47), 11353-11365.

975 Simon, H. & Lumsden, A. (1993). Rhombomere-specific origin of the contralateral vestibulo-acoustic
976 efferent neurons and their migration across the embryonic midline. Neuron *11*, 209-220.

977 Steinberg, M. S. & Takeichi, M. (1994). Experimental specification of cell sorting, tissue spreading,
978 and specific spatial patterning by quantitative differences in cadherin expression. PNAS 91, 206–9.

979 Sürmeli, G., Akay, T., Ippolito, G. C., Tucker, P. W. & Jessell, T. M. (2011). Patterns of Spinal
980 Sensory-Motor Connectivity Prescribed by a Dorsoventral Positional Template. Cell, *147*, 653-665.

981 Taniguchi, H., Tamada, A., Kennedy, T. E., Murakami, F. (2002). Crossing the Ventral Midline Causes
982 Neurons to Change Their Response to Floor Plate and Alar Plate Attractive Cues during Transmedian
983 Migration. Developmental Biology *249*, 321-332.

984 Tripodi, M., Stepien, A. E. & Arber, S. (2011). Motor antagonism exposed by spatial segregation and
985 timing of neurogenesis. Nature, *64*(479), 61-68.

986 Vanderhorst, V., & Holstege, G. (1997). Organization of lumbosacral motoneuronal cell groups
987 innervating hindlimb, pelvic floor, and axial muscles in the cat. Journal of Comparative Neurology
988 *382*(1), 46–76.

989 Wanner, S. J. & Prince, (2013). Axon tracts guide zebrafish facial branchiomotor neuron migration
990 through the hindbrain. Development *140*, 906-915.

991 Warp, E., Agarwal, G., Wyart, C., Friedmann, D., Oldfield, C., Conner, A., Del Bene, F., Arrenberg, A.
992 B., Baier, H. & Isacoff, E. Y. (2012). Emergence of Patterned Activity in the Developing Zebrafish
993 Spinal Cord. Current Biology *22*(2), 93–102.

994 Ypsilanti, A. R., Zagar, Y., Chédotal, A. (2010). Moving away from the midline: new developments for
995 Slit and Robo. Development *137*, 1939-1952.

996

997

998

999

1000

Figure titles and legends

Figure 1. Differential expression of cadherin combinations in ocular motor neurons in *Isl1:GFP* zebrafish at 48 hpf.
(A) Dorsal view of cranial motor neurons (green) and *cdh8* expression (magenta). Abbreviations: MB, midbrain; HB, hindbrain; r1-8, rhombomeres 1-8; nIII, oculomotor nucleus; nIV, trochlear nucleus; nVa, anterior trigeminal nucleus; nVp, posterior trigeminal nucleus; nVII, facial motor nucleus. Dotted lines indicate MHB, midline and outlines of the neural tube.
(B-C) Combinatorial cadherin expression in nIV and nIII neurons. Small, regular and large fonts indicate low, normal and high expression levels. Views represent flattened dorsal and transverse projections. IR, inferior rectus; MR, medial rectus; SR, superior rectus; IO, inferior oblique. See also Figure 1-figure supplements 1 and 2.
(D-K) Expression of type I cadherins *cdh2* and *cdh4* and type II cadherins *cdh8* and *cdh10a* (magenta) in ocular motor neurons (green). White and blue arrows indicate high and low expression, outlines indicate location of nIII and nIV. All images are snapshots of 3D Imaris visualisations of entire z-stacks. Scale bars = 20μm.
(D-G) Dorsal views of ocular motor neurons and cadherin expression in surrounding tissue and masked by GFP-positive area.
(H-K) Transverse views of ocular motor neurons and masked cadherin expression by GFP-positive area.

Figure 1-figure supplement 1. Differential expression of cadherins in ocular motor neurons in *Isl1:GFP* at 48 hpf.
(A-B) Dorsal views of ocular motor neurons (green) and detection of mRNA expression (magenta) of *dapB* (A, negative control) and *foxg1a* (B, positive control).
(C-E) Expression of type II cadherins *cdh7a* and *cdh11* and atypical cadherin *cdh13* (magenta) in ocular motor neurons (green). Dorsal views show cadherin expression in surrounding tissue and masked by GFP-positive area. Outlines indicate locations of nIII and nIV. White and blue arrows indicate high and low expression, respectively. All images represent snapshots of 3D Imaris visualisations of entire z-stacks. Scale bars (A, C-E) = 20μm.

Movie 1. Expression of *cdh8* (magenta) in ocular motor neurons (green) in *Tg(Isl1:GFP)* embryo at 48 hpf in confocal z-stack. Movie displays z-stack moving from most ventral to dorsal and reveals high ventral expression.

Movie 2. Expression of *cdh7a* (magenta) in ocular motor neurons (green) in *Tg(Isl1:GFP)* embryo at 48 hpf in confocal z-stack. Movie displays z-stack moving from most ventral to dorsal and reveals low ventral expression.

Figure 1-figure supplement 2. Differential expression of cadherin combinations in ocular motor neurons in *Isl1:GFP* at 72 hpf.
(A-B) Summary schematics of combinatorial cadherin expression in nIV and nIII neurons based on anatomical location. Small, regular and large fonts indicate low, normal and high expression levels. Views represent flattened dorsal and transverse projections. IR, inferior rectus; MR, medial rectus; SR, superior rectus.
(C-I) Expression of type I cadherins *cdh2* and *cdh4*, type II cadherins *cdh7a*, *cdh8*, *cdh10a* and *cdh11* and atypical cadherin *cdh13* (magenta) in ocular motor neurons (green) and surrounding tissue. Dorsal views show cadherin expression in surrounding tissue and masked by GFP-positive area. Outlines indicate locations of nIII and nIV. White and blue arrows indicate high and low expression, respectively. All images represent snapshots of 3D Imaris visualisations of entire z-stacks. Scale bars = 20μm.

1056 **Figure 2. Expression of *cdh2ΔEC* in zebrafish ocular motor neurons causes scattering of dorsal**
1057 **oculomotor neurons.**
1058 (A-B) Dorsal MIPs of nIII and nIV (green) in wild-type (A) *Isl1:GFP* and *cdh2ΔEC* larvae (B) at 72 hpf.
1059 Arrows point to dorsal neurons which lie in lateral regions of nIII. TN, trochlear nerve. Scale bars =
1060 20μm. See also Figure 2-figure supplement 1.
1061 (C-E') Oculomotor coordinates in dorsal half of nIII shown in dorsal and lateral views of wild-type
1062 *Isl1:GFP* and *cdh2ΔEC* larvae at 72 hpf, colour coded according to z-level. Arrows point to dorsal nIII
1063 neurons which are mispositioned in *cdh2ΔEC* fish. All images are snapshots of 3D Imaris visualisations
1064 of entire z-stacks. Outlines indicate location of nIV. Scale bars = 20μm.
1065 (F) Convex hull volumes of dorsal cell coordinates. Data represents median and range, n = 6 larvae
1066 from two clutches for each genotype, *p = 0.0411, 2-tailed Mann-Whitney U.
1067 (G) Local cell densities derived from dorsal cell coordinates. Data represents median and range, n = 6
1068 larvae from two clutches for each genotype, *p = 0.0152. There was no significant difference in the
1069 number of cells measured per side (medians of 28.25 for wild-types and 29.75 for *cdh2ΔEC*; n=6 larvae
1070 per genotype, p = 0.3074). Both tests are 2-tailed Mann-Whitney U.
1071
1072
1073 **Figure 2-figure supplement 1. Ocular motor nuclei of *cdh2ΔEC* larvae retain key characteristics**
1074 **of dorsoventral organisation but appear disorganised compared to wild-types.**
1075 (A, B) Dorsal views of the entire z-stack for representative wild-type *Isl1:GFP* and *cdh2ΔEC* larvae at
1076 72 hpf. Example embryo in (B) is the same as shown in Figure 2D.
1077 (A'-A''''; B'-B'''') Sub-stack projections of 3 combined dorsoventral (DV) subdivisions (z0-z14) moving
1078 from dorsal to ventral for wild-type *Isl1:GFP* (A-A'''') and *cdh2ΔEC* (B-B'''') larvae. All images are
1079 maximum intensity projections of confocal z-stacks. nIII: rostral to MHB; nIV: caudal to MHB. Arrows
1080 indicate differences in clustering of dorsal neurons and less organised ventral population in the case of
1081 *cdh2ΔEC* larvae. MHB: midbrain-hindbrain boundary, mid: midline. Scale bars = 20μm.
1082
1083
1084 **Figure 3. Contralateral migration of ventral SR neurons is abolished in *cdh2ΔEC* fish.**
1085 (A) Dorsal view schematic of contralateral migration phases. Dotted lines and arrows indicate the
1086 midline and direction of migration, lines represent leading processes.
1087 (B) Transverse view of an *Isl1:GFP* embryo immunostained against GFP. TN, trochlear nerve. Scale
1088 bars = 20μm.
1089 (C-D) MIPs of ventral half of wild-type *Isl1:GFP* and *cdh2ΔEC* embryos immunostained against GFP
1090 and RFP at 50 hpf. Dotted lines represent the midline.
1091 (E-F) Single sagittal sections of nIII GFP fluorescence at the midline in wild-type and *cdh2ΔEC* fish.
1092 Scale bars = 20μm.
1093 (G) Area of GFP fluorescence measured in sagittal sections of nIII. Error bars represent median and
1094 range, n = 7 (wild-type) from two clutches and n = 14 from two clutches (*cdh2ΔEC*), *p = 0.0125. There
1095 was no difference in the number of nIII cells (medians for wild-types (n=4) = 95 and *cdh2ΔEC* (n=9) =
1096 103, p=0.414). Both tests are 2-tailed Mann-Whitney U.
1097 (H) Labelling of ocular motor subnuclei by retro-orbital dye fill. MHB, midbrain-hindbrain boundary.
1098 (I-J') Ventral MIPs of DiI-filled ventral nIII neurons in *Isl1:GFP* and *cdh2ΔEC* larvae at 5 dpf. Scale bars
1099 = 20μm. White arrows indicate neurons which have crossed to the contralateral side, asterisks
1100 represent mCherry+ signal.
1101 (K-L'') Dorsal MIPs of sparsely labelled neurons located in ventral nIII in *Isl1:GFP* and *cdh2ΔEC* larvae
1102 at 5 dpf. White and blue arrows indicate GFP-positive and GFP-negative dye-filled neurons. The left
1103 eye is the side of dye fill. Alx647 = AlexaFluor 647 dye. Scale bars = 20μm. Note that in K-K'', small
1104 magenta puncta represent non-specific dye spread, while in K-K'' these likely also include punctate
1105 mCherry signal from *cdh2ΔEC* expression, due to spectral overlap.
1106 (M) Total observed number of pooled dye-filled cells belonging to each category in wild-types and
1107 *cdh2ΔEC* at 5 dpf. There is a significant relationship between genotype and distribution of dye-filled
1108 neurons, (p<0.0001; chi squared test). There was no significant effect of genotype on the total number
1109 of dye-filled neurons across groups per larva, medians for wild-types = 31, *cdh2ΔEC* = 40.5, p=0.674,
1110 2-tailed Mann-Whitney U. Wild-type larvae are from four clutches and *cdh2ΔEC* larvae are from five
1111 clutches.

(N-Q) Percentage proportions of dye-filled neurons per larva for each genotype separated by category. All tests are 2-tailed Mann-Whitney U.

(N) Percentage proportions of contralateral GFP-positive SR cells. n = 15 larvae (wild-type) and n = 16 (*cdh2ΔEC*) larvae, **p = 0.0015.

(O) Percentage proportions of ipsilateral GFP+ cells. n = 15 larvae (wild-type) and n = 16 (*cdh2ΔEC*) larvae, *p = 0.0109.

(P) Percentage proportions of ipsilateral GFP negative IO cells. n = 15 larvae (wild-type) and n = 16 (*cdh2ΔEC*) larvae, p = 0.5131.

(Q) Percentage proportions of contralateral nIV cells. n = 19 larvae (wild-type) and n = 20 (*cdh2ΔEC*) larvae, p = 0.9391.

(N-P) Proportions are relative to the total number of nIII cells filled per larva, for (Q) proportions are relative to combined total of dye-filled nIII and nIV neurons. Larvae in which less than 10 nIII cells were filled in total were excluded from analysis in (N-P), whereas larvae in which less than 10 combined nIII & nIV cells were filled in total were excluded from analysis in (Q).

Figure 4. *cdh2ΔEC* expression results in mispositioning of zebrafish trochlear neurons along the dorsoventral axis.

(A-B) Lateral view MIPs of nIII and nIV of wild-type *lsl1:GFP* and *cdh2ΔEC* larvae at 72 hpf. Dotted lines represent the midbrain-hindbrain boundary. OMN, oculomotor nerve; TN, trochlear nerve.

(C) Measurements of dorsoventral extent of nIV at 72 hpf. Dots represent individual larvae. Error bars represent median and range. n=14 larvae from two clutches for each genotype, **p=0.0042, 2-tailed Mann-Whitney U.

Figure 5. Non-*cdh2ΔEC* expressing zebrafish inferior oblique neurons are mispositioned following perturbation of cadherin function in neighbouring oculomotor subnuclei.

(A-A") Transverse MIP of a wild-type *lsl1:GFP* larva at 5 dpf in which nIII and nIV neurons have been labelled using retro-orbital dye fills with Alexa647 dextrans. Ipsi denotes side of dye fill. White and yellow arrows indicate ipsilateral GFP-negative IO neurons and ipsilateral GFP-positive neurons (IR/MR). Blue and orange arrows indicate contralateral GFP-positive SR neurons and SO (nIV) neurons. OMN, oculomotor nerve; TN, trochlear nerve. Scale bars = 20μm.

(B-C) Normalised empirical and posterior (E-F) probability distribution of IO neuron spatial locations in wild-types (278 cells, n=19 larvae, four clutches) and *cdh2ΔEC* (399 cells, n=22 larvae, five clutches) according to dorsoventral (DV; from z0 (ventral) to z14 (dorsal)) and mediolateral (ML; from x0 (medial) to x3 (lateral)) subdivisions.

(D) Normalised empirical and posterior (G) differential probability distribution of IO neuron spatial locations between genotypes. diff = *cdh2ΔEC* distribution – wild-type distribution. There are differences in the overall spatial distribution between genotypes (KL_{mean}=0.3114, 95% CI [0.3107 0.3122]).

(H-I) Median posterior probabilities of IO cell location within DV (H) and ML (I) subdivisions for wild-types and *cdh2ΔEC* larvae. There is a difference in DV (*z-shift* = 0.5201, 95% CI [0.5168 0.5234]) and ML distribution (*x-shift* = -0.1423, 95% CI [-0.1431 -0.1414]) between genotypes.

(J-K) Diagrammatic representation of transverse and lateral views of IO ocular motor neuron location in wild-types and *cdh2ΔEC.* Perturbation of cadherin binding between *cdh2ΔEC*-expressing IR/MR and SR subnuclei and wild-type IO neurons leads to a ventral and lateral shift in IO neuron location.

Figure 6. Extraocular muscle innervation and neuromuscular junction formation is unperturbed in *cdh2ΔEC* larvae.

(A-B) Immunostained axon projections of oculomotor and trochlear nerves (α-tubulin) innervating extraocular muscles (myosin heavy chain) at 72 hpf in wild-types and *cdh2ΔEC-mCherry.* Images are lateral view MIPs, white arrow indicates the point at which the oculomotor nerve enters the orbit. Boxes show high magnification view of individual branches. Scale bars = 40μm. (C) Quantification of branch number per genotype for each nerve/branch. There was no significant difference in branch number for any muscle target (ns; SR, p=0.9406; MR, p=0.9451; IR, p=0.8512; IO, p=0.9451; SO, p=0.94512;

1167 multiple t-tests, and Holm-Sidak test). Error bars are mean and SD. Both wild-type and *cdh2ΔEC* larvae
1168 are from three clutches.
1169 (D-G'') Immunostained NMJs composed of presynaptic vesicles (SV2) and acetylcholine receptors (α-
1170 bungarotoxin) in wild-types (D-E'') and *cdh2ΔEC* (F-G'') at 4 dpf at the medial rectus (MR) muscle.
1171 Scale bars = 20μm. All images are MIPs of sub-stacks taken from larger z-stacks. See also Figure 6-
1172 figure supplement 1.
1173
1174
1175 **Figure 6-figure supplement 1. Perturbation of cadherin function does not disrupt zebrafish**
1176 **extraocular neuromuscular junction formation.**
1177 (A-H'') Immunostained NMJs composed of presynaptic vesicles (SV2) and acetylcholine receptors (α-
1178 bungarotoxin) in wild-type (A-D'') and *cdh2ΔEC* (E-H'') larvae at superior rectus (SR), inferior rectus
1179 (IR), inferior oblique (IO) and superior oblique (SO) extraocular muscles at 4 dpf. Scale bars = 20μm.
1180 All images are MIPs of sub-stacks taken from larger z-stacks.
1181 (I) Area of SV2+ signal and colocalisation coefficient of SV2 and α-bungarotoxin (J) of NMJs of each
1182 individual extraocular muscle. There was no significant difference in the area of SV2 (SR, p=0.9880;
1183 MR, p=0.9391; IR, p=0.9880; IO, p=0.9880; SO, p=0.9751; multiple t-tests, and Holm-Sidak test) or
1184 colocalization of SV2 (SR, p=0.9288; MR, p=0.9288; IR, p=0.9212; IO, p=0.9288; SO, p=0.9534) and
1185 α-bungarotoxin for any muscle between wild-types (n=7 for SR, MR, IR, IO; n=6 for SO; from two
1186 clutches) and *isl1:cdh2ΔEC-mCherry* (n=7 for MR, IO, SO; n=6 for SR and IR; from two clutches). Error
1187 bars are mean and SD.
1188
1189
1190 **Figure 7. *cdh2ΔEC* larvae display impaired efficiency of nasal eye movements and defects in**
1191 **eye range.**
1192 (A-A') Example OKR movie still illustrating coordinated nasal (right eye) and temporal (left eye) eye
1193 movements.
1194 (B) Ocular motor circuitry of underlying the OKR of larval zebrafish. Nasal and temporal eye movements
1195 are driven by medial and lateral rectus-innervating motor neurons of distinct nuclei.
1196 (C-D) Average nasal (C) and temporal (D) eye gain of wild-types and *cdh2ΔEC* larvae averaged for all
1197 trials. There is a significant difference in nasal eye gain for the strong (p=0.0003) and weak eye
1198 (p=0.0472). There was no significant difference in temporal eye gain for the strong (p=0.0597) or weak
1199 eye (p=0.2574).
1200 (E) Total eye range for strong and weak eyes for each genotype. There was a significant difference for
1201 the strong (p<0.0001) and weak eye (p=0.0011).
1202 (C-E) All tests are t-test with Welch's corrections. Error bars are mean and SD. Both wild-type and
1203 *cdh2ΔEC* larvae are from two clutches.
1204